

AD-A107 962

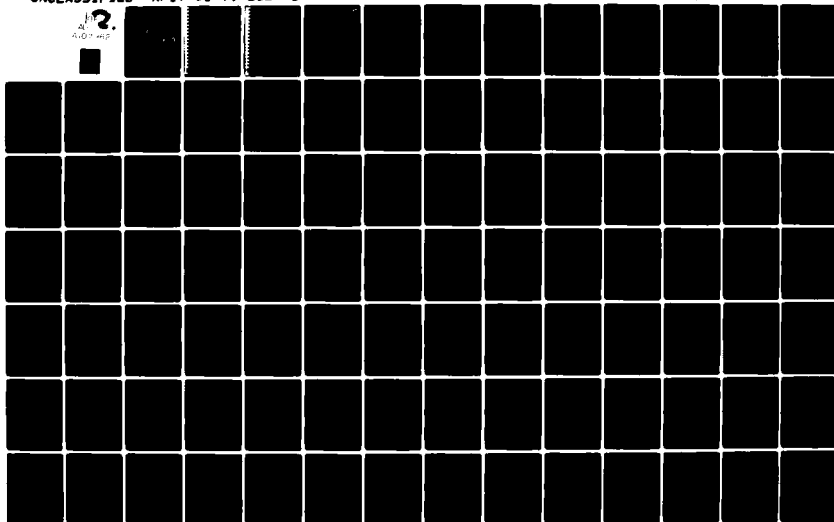
AIR FORCE INST OF TECH WRIGHT-PATTERSON AFB OH
EFFECTS OF PRECIPITATING AND NONPRECIPITATING CLOUD LAYERS ON T--ETC(U)
JUN 79 P T NIPKO
AFIT-CI-79-282T-S

F/G 4/2

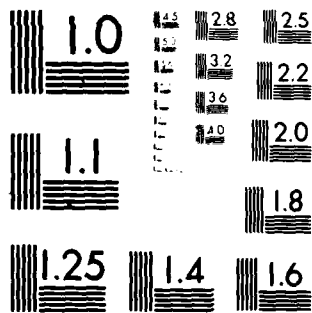
UNCLASSIFIED

NL

2.
AL
4/01-101



0796



MICROCOPY RESOLUTION TEST CHART
NATIONAL BUREAU OF STANDARDS-1963-A

REPORT DOCUMENTATION PAGE		READ INSTRUCTIONS BEFORE COMPLETING FORM
1. REPORT NUMBER 79-2821-S	2. GOVT ACCESSION NO. AD-A187	3. RECIPIENT'S CATALOG NUMBER 162
4. TITLE (and Subtitle) Effects of Precipitating and Nonprecipitating Cloud Layers on the Defense Meteorological Satellite Program		5. TYPE OF REPORT & PERIOD COVERED THESIS/DISSERTATION
7. AUTHOR(s) Paul Thomas Nipko		6. PERFORMING ORG. REPORT NUMBER
9. PERFORMING ORGANIZATION NAME AND ADDRESS AFIT STUDENT AT: Univ of Utah		8. CONTRACT OR GRANT NUMBER(s)
11. CONTROLLING OFFICE NAME AND ADDRESS AFIT/NR WPAFB OH 45433		10. PROGRAM ELEMENT, PROJECT, TASK AREA & WORK UNIT NUMBERS
14. MONITORING AGENCY NAME & ADDRESS (if different from Controlling Office) LEVEL III		12. REPORT DATE Jun 1979
		13. NUMBER OF PAGES 85
		15. SECURITY CLASS. (of this report) UNCLASS
		15a. DECLASSIFICATION/DOWNGRADING SCHEDULE
16. DISTRIBUTION STATEMENT (of this Report) APPROVED FOR PUBLIC RELEASE; DISTRIBUTION UNLIMITED		
17. DISTRIBUTION STATEMENT (of the abstract entered in Block 20, if different from Report) 23 NOV 1981		
18. SUPPLEMENTARY NOTES APPROVED FOR PUBLIC RELEASE: IAW AFR 190-17 FREDRIC C. LYNCH, Major, USAF Director of Public Affairs Air Force Institute of Technology (AIC) Wright-Patterson AFB, OH 45433		
19. KEY WORDS (Continue on reverse side if necessary and identify by block number)		
20. ABSTRACT (Continue on reverse side if necessary and identify by block number) ATTACHED		

DD FORM 1 JAN 73 1473 EDITION OF 1 NOV 65 IS OBSOLETE

UNCLASS

SECURITY CLASSIFICATION OF THIS PAGE (When Data Entered)

AD A107962

DTIC FILE COPY

ABSTRACT

This study is a sensitivity analysis of the Defense Meteorological Satellite Program (DMSP) Block 5D Passive Temperature Sounder (SSM/T) to intervening cloud layers. Brightness temperatures for each of the seven SSM/T channels are calculated based upon two different climatological profiles. Intervening precipitating and nonprecipitating cloud layers are simulated using drop size distributions based upon rainfall rate and Deirmendjian's L-Model cloud, respectively. Radiative transfer through these layers is approximated using the discrete ordinate method for sixteen discrete streams. The effects of such layers on calculated brightness temperatures are shown to vary with cloud position, thickness and precipitation rate. The importance of the variation in the earth's emissivity between land and ocean surfaces is demonstrated. Not only do such variations cause changes in brightness temperature values, but general trends for individual channels are altered. The relative importance of atmospheric, surface emission and cloud effects is broken out for the Mid-Latitude Spring/Fall profile over ocean.

The effects of resulting brightness temperature variations on the Air Force Global Weather Central (AFGWC) statistical temperature retrieval technique and Chahine's relaxation technique are also presented. The accuracy of the AFGWC and Chahine temperature retrieval schemes is demonstrated by comparing the clear column retrievals to the actual

profiles. The degradation due to intervening clouds are then demonstrated by presenting the temperature profiles retrieved based upon the brightness temperatures calculated for the cloudy cases.

Accession For	
NTIS GRA&I	<input checked="checked" type="checkbox"/>
DTIC TAB	<input type="checkbox"/>
Unannounced	<input type="checkbox"/>
Justification	
By	
Distribution/	
Availability Codes	
Avail and/or	
Dist	Special
A	

~~SECRET~~
7-285-5

EFFECTS OF PRECIPITATING AND NONPRECIPITATING CLOUD LAYERS
ON THE DEFENSE METEOROLOGICAL SATELLITE PROGRAM
MICROWAVE TEMPERATURE SOUNDER

by
Paul Thomas Nipko

A thesis submitted to the faculty of The
University of Utah in partial fulfillment of the
requirements for the degree of

Master of Science

Department of Meteorology
The University of Utah
June 1979

81 11 30 008

THE UNIVERSITY OF UTAH GRADUATE SCHOOL

SUPERVISORY COMMITTEE APPROVAL

of a thesis submitted by

Paul T. Nipko

I have read this thesis and have found it to be of satisfactory quality for a master's degree.

April 9, 1979
Date

Kuo-Nan Liou
Kuo-Nan Liou
Chairman, Supervisory Committee

I have read this thesis and have found it to be of satisfactory quality for a master's degree.

April 9, 1979
Date

S. K. Kao
S. K. Kao
Member, Supervisory Committee

I have read this thesis and have found it to be of satisfactory quality for a master's degree.

April 9, 1979
Date

Elford G. Astling
Elford G. Astling
Member, Supervisory Committee

THE UNIVERSITY OF UTAH GRADUATE SCHOOL

FINAL READING APPROVAL

To the Graduate Council of The University of Utah:

I have read the thesis of Paul T. Nipko in its final form and have found that (1) its format, citations, and bibliographic style are consistent and acceptable; (2) its illustrative materials including figures, tables, and charts are in place; and (3) the final manuscript is satisfactory to the Supervisory Committee and is ready for submission to the Graduate School.

April 9, 1979

Date

Kuo-Nan Liou

Kuo-Nan Liou

Member, Supervisory Committee

Approved for the Major Department

S. K. Kao

S. K. Kao

Chairman/Dean

Approved for the Graduate Council

James L. Clayton

Dean of The Graduate School

ABSTRACT

This study is a sensitivity analysis of the Defense Meteorological Satellite Program (DMSP) Block 5D Passive Temperature Sounder (SSM/T) to intervening cloud layers. Brightness temperatures for each of the seven SSM/T channels are calculated based upon two different climatological profiles. Intervening precipitating and nonprecipitating cloud layers are simulated using drop size distributions based upon rainfall rate and Deirmendjian's L-Model cloud, respectively. Radiative transfer through these layers is approximated using the discrete ordinate method for sixteen discrete streams. The effects of such layers on calculated brightness temperatures are shown to vary with cloud position, thickness and precipitation rate. The importance of the variation in the earth's emissivity between land and ocean surfaces is demonstrated. Not only do such variations cause changes in brightness temperature values, but general trends for individual channels are altered. The relative importance of atmospheric, surface emission and cloud effects is broken out for the Mid-Latitude Spring/Fall profile over ocean.

The effects of resulting brightness temperature variations on the Air Force Global Weather Central (AFGWC) statistical temperature retrieval technique and Chahine's relaxation technique are also presented. The accuracy of the AFGWC and Chahine temperature retrieval schemes is demonstrated by comparing the clear column retrievals to the actual

profiles. The degradation due to intervening clouds are then demonstrated by presenting the temperature profiles retrieved based upon the brightness temperatures calculated for the cloudy cases.

TABLE OF CONTENTS

	<u>Page</u>
ABSTRACT	iv
LIST OF FIGURES	viii
LIST OF TABLES	xi
ACKNOWLEDGEMENTS	xii
 CHAPTER	
1. INTRODUCTION	1
2. CHARACTERISTICS OF SSM/T CHANNELS	4
3. OPTICAL PARAMETERS FOR SSM/T CHANNELS	11
3.1 Mie Theory	11
3.2 Indices of Refraction	11
3.3 Drop Size Distributions	13
3.4 Parameter Values	13
4. MICROWAVE RADIATIVE TRANSFER	26
4.1 Clear Column Brightness Calculations	26
4.2 Brightness Calculations for Cloudy Atmospheres . .	31
5. SENSITIVITY TO CLOUD LAYERS	35
5.1 Profiles and Cloud Models Used	35
5.2 Dependence on Layer Thickness and Rainfall Rate .	38
5.2.1 Over Land	40
5.2.2 Over Ocean	40
5.3 Dependence on Layer Location	42
5.4 Dependence on Profile	42
5.5 Interpretation of Results	43
6. TEMPERATURE RETRIEVALS	68
6.1 AFGWC Statistical Method	68
6.2 Chahine's Relaxation Method	72
6.3 Presentation of Results	74

	<u>Page</u>
7. CONCLUSION	81
REFERENCES	83
VITA	85

LIST OF FIGURES

Figure	<u>Page</u>
1. SSM/T scan geometry. Source: Riogone and Stogryn (1977)	5
2. SSM/T weighting functions (nadir) with antenna gain characteristics included ($\epsilon = .97$)	7
3. Brightness temperature vs rainfall rate (or liquid water content) for 1 Km thick cloud over land (Mid-Latitude Spring/Fall profile).	49
4. Brightness temperature vs rainfall rate (or liquid water content) for 2 Km thick cloud over land (Mid-Latitude Spring/Fall profile)	49
5. Brightness temperature vs rainfall rate (or liquid water content) for 3 Km thick cloud over land (Mid-Latitude Spring/Fall profile).	50
6. Brightness temperature vs rainfall rate (or liquid water content) for 4 Km thick cloud over land (Mid-Latitude Spring/Fall profile)	50
7. Brightness temperature vs rainfall rate (or liquid water content) for 5 Km thick cloud over land (Mid-Latitude Spring/Fall profile)	51
8. 50.50 GHz brightness temperature as a function of cloud thickness and liquid water content (Mid-Latitude Spring/Fall profile over ocean)	52
9. 53.20 GHz brightness temperature as a function of cloud thickness and liquid water content (Mid-Latitude Spring/Fall profile over ocean)	52
10. 54.35 GHz brightness temperature as a function of cloud thickness and liquid water content (Mid-Latitude Spring/Fall profile over ocean)	53
11. 54.90 GHz brightness temperature as a function of cloud thickness and liquid water content (Mid-Latitude Spring/Fall profile over ocean)	53

Figure	Page
12. 50.50 GHz brightness temperature dependence on cloud base height for a 2 Km thick Deirmendjian L-Model cloud (Mid-Latitude Spring/Fall profile over land)	54
13. 53.20 GHz brightness temperature dependence on cloud base height for a 2 Km thick Deirmendjian L- Model cloud (Mid-Latitude Spring/Fall profile over land)	54
14. 54.35 GHz brightness temperature dependence on cloud base height for a 2 Km thick Deirmendjian L-Model cloud (Mid-Latitude Spring/Fall profile over land)	55
15. 54.90 GHz brightness temperature dependence on cloud base height for a 2 Km thick Deirmendjian L-Model cloud (Mid-Latitude Spring/Fall profile over land)	55
16. 58.82 GHz brightness temperature dependence on cloud base height for a 2 Km thick Deirmendjian L-Model cloud (Mid-Latitude Spring/Fall profile over land)	56
17. 59.40 GHz brightness temperature dependence on cloud base height for a 2 Km thick Deirmendjian L-Model cloud (Mid-Latitude Spring/Fall profile over land)	56
18. 50.50 GHz brightness temperature dependence on cloud base height for a 2 Km thick Deirmendjian L-Model cloud (Mid-Latitude Spring/Fall profile over ocean)	57
19. 53.20 GHz brightness temperature dependence on cloud base height for a 2 Km thick Deirmendjian L-Model cloud (Mid-Latitude Spring/Fall profile over ocean)	57
20. 54.35 GHz brightness temperature dependence on cloud base height for a 2 Km thick Deirmendjian L-Model cloud (Mid-Latitude Spring/Fall profile over ocean)	58
21. 54.90 GHz brightness temperature dependence on cloud base height for a 2 Km thick Deirmendjian L-Model cloud (Mid-Latitude Spring/Fall profile over ocean)	58
22. 58.82 GHz brightness temperature dependence on cloud base height for a 2 Km thick Deirmendjian L-Model cloud (Mid-Latitude Spring/Fall profile over ocean)	59
23. 59.40 GHz brightness temperature dependence on cloud base height for a 2 Km thick Deirmendjian L-Model cloud (Mid-Latitude Spring/Fall profile over ocean)	59

Figure	Page
24. 50.50 GHz channel profile dependence over land	60
25. 53.20 GHz channel profile dependence over land	60
26. 54.35 GHz channel profile dependence over land	61
27. 54.90 GHz channel profile dependence over land	61
28. 50.50 GHz channel profile dependence over ocean	62
29. 53.20 GHz channel profile dependence over ocean	63
30. 54.35 GHz channel profile dependence over ocean	64
31. 54.90 GHz channel profile dependence over ocean	64
32. Radiative transfer through a cloud layer	65
33. Component contributions to 50.50 GHz cloud top bright- ness for a 1 Km thick cloud over ocean (Mid-Latitude Spring/Fall profile)	66
34. Component contributions to 50.50 GHz cloud top bright- ness for a 3 Km thick cloud over ocean (Mid-Latitude Spring/Fall profile)	66
35. Component contributions to 53.20 GHz cloud top bright- ness for a 1 Km thick cloud over ocean (Mid-Latitude Spring/Fall profile)	67
36. Component contributions to 53.20 GHz cloud top bright- ness for a 3 Km thick cloud over ocean (Mid-Latitude Spring/Fall profile)	67
37. AFGWC temperature retrieval over land (Mid-Latitude Spring/Fall profile)	76
38. AFGWC temperature retrieval over ocean (Mid-Latitude Spring/Fall profile)	77
39. Chahine temperature retrieval over land (Mid-Latitude Spring/Fall profile)	78
40. Chahine temperature retrieval over ocean (Mid-Latitude Spring/Fall profile)	79

LIST OF TABLES

Table	<u>Page</u>
1. Channel Parameter Design Specifications	5
2. Scan Parameters	6
3. Percent Gains Averaged Over Bore Sight Angles	8
4. Refractive Index ($m=m_r-im_i$) of Pure Liquid Water	12
5. Refractive Index of Pure Liquid Water (SSM/T)	12
6. Optical Parameters (Deirmendjian L-Model)	15
7. Optical Parameters (Marshall-Palmer 1 mm/hr).	16
8. Optical Parameters (Marshall-Palmer 2 mm/hr).	17
9. Optical Parameters (Marshall-Palmer 3 mm/hr).	18
10. Optical Parameters (Marshall-Palmer 4 mm/hr).	19
11. Optical Parameters (Marshall-Palmer 5 mm/hr).	20
12. Optical Parameters (Marshall-Palmer 10 mm/hr)	21
13. Optical Parameters (Marshall-Palmer 15 mm/hr)	22
14. Optical Parameters (Marshall-Palmer 20 mm/hr)	23
15. Optical Parameters (Marshall-Palmer 25 mm/hr)	24
16. Optical Parameters (Marshall-Palmer 30 mm/hr)	25
17. N. Hemisphere Mid-Latitude Spring/Fall Profile	36
18. 30°N. Latitude July Profile	37
19. Total Liquid Water Content	39

ACKNOWLEDGEMENTS

I wish to thank Dr. Kou-Nan Liou without whose guidance and support this thesis would not have been possible.

I also wish to express my appreciation to Mr. Stogryn of Aerojet General for providing the gain characteristics of the SSM/T and to Maj Savage of AFGWC for providing the statistical temperature retrieval program analysed in this study.

Finally, I would like to thank my wife, Anita, for her patience and encouragement during this research.

This research was supported by the Air Force Geophysics Laboratory under Contract F19628-78-C-0144.

CHAPTER 1

INTRODUCTION

Determination of atmospheric temperature structure from satellite sensed atmospheric thermal emission was first suggested by King (1956). Kaplan (1959) advanced the concept by demonstrating that vertical resolution could be obtained from the spectral distribution of atmospheric emission; observations in more transparent regions of the spectrum sense deeper into the atmosphere. In order for atmospheric temperatures to be determined by measurements of thermal emission, the source of emission must be a relatively abundant gas of known and uniform distribution. Carbon dioxide, a minor constituent with a relative volume abundance of .003 and oxygen, a major constituent with a relative volume abundance of .21, satisfy this requirement. Carbon dioxide absorbs in an infrared vibrational-rotational band while oxygen absorbs in a microwave spin-rotational band.

At first the 15 μm CO_2 infrared band was used for all satellite experiments to determine the atmospheric temperature profiles. The higher energy infrared radiation could be measured by a much smaller sensor; an important consideration for satellite born systems. From 1963 to 1972 a variety of infrared sensors were flown on several different spacecraft. Although, the soundness of the theory behind remotely sensing the temperature profile was clearly demonstrated, one major problem continues to exist. Global atmospheric temperature

profile coverage can not be obtained due to the effects of clouds and precipitation upon infrared radiation. Several sophisticated techniques have been developed in an attempt to eliminate these effects (Smith et. al., 1970; Rodgers, 1970; Chahine, 1970, 1974), none of which are valid under all conditions encountered within the atmosphere.

The primary advantage of microwave temperature sounders over infrared sounders is that the longer microwaves are much less effected by clouds and precipitation. The determination of atmospheric temperatures from satellite measured microwave radiation was first suggested by Meeks (1961). Ten years later the first Microwave Spectrometer experiment (NEMS) was flown aboard Nimbus 5. The accuracy with which microwave techniques could provide vertical temperature profiles was shown to be quite good (Waters et. al., 1975). Furthermore, only 0.5% of all NEMS temperature soundings were measurably effected by clouds and most of these occurred in the ITCZ (Staelin et. al., 1975). The major purpose of the NEMS experiment was to evaluate passive microwave techniques for use on operational meteorological satellites. It was not intended for operational use itself, and had only three channels which responded primarily to the atmospheric temperature profile. Of these only channel 3 (53.65GHz) penetrated the atmosphere deeply enough to be significantly effected by clouds.

The first microwave sensor intended for operational use is to be flown aboard the DMSP Block 5D satellite system scheduled to be launched in 1979. This microwave sensor (SSM/T) contains seven channels, four of which have weighting functions peaking near or below 10 km. These four channels penetrate deeply enough into the atmosphere to be effected by clouds and precipitation. The purpose of this study is to

analytically determine what brightness temperature variations could be expected and how such variations will impact the operational temperature retrieval scheme to be used by the Air Force Global Weather Central (AFGWC).

Chapter 2 describes the characteristics of the SSM/T channels. Chapter 3 details the optical parameters used and the cloud and precipitation models from which they were obtained. Chapter 4 describes the solution of the radiative transfer through the cloud or precipitation layer. Chapter 5 displays the clear column calculations for the two model profiles used and the changes in brightness temperatures which result from clouds and precipitation. Chapter 6 describes the AFGWC temperature retrieval scheme and how the forementioned variations in brightness temperature impact this scheme.

CHAPTER 2

CHARACTERISTICS OF SSM/T CHANNELS

The SSM/T sounder system operates in the oxygen absorption band at frequencies of 50.5, 53.2, 54.35, 54.9, 58.4, 58.825 and 59.4 GHz. The sensor is a crosstrack scanning radiometer which acquires data at 32-second intervals at 7 angular positions separated by 12 degrees (see Figure 1.). Channel 1 is a window channel responding strongly to the earth's surface characteristics. It is used to correct the other channels for these background effects. Microwave data are acquired by means of a mechanically scanning, shrouded-reflector antenna system. The channel parameter design specifications are presented in Table 1 and the scan parameters are illustrated in Table 2. The seven SSM/T channels have been selected such that the weighting functions peak at different altitudes within the atmosphere providing the necessary vertical resolution for temperature profile retrieval. The weighting functions for each channel are displayed in Figure 2. These weighting functions result from consideration of atmospheric absorption due to water vapor and molecular oxygen with transmissivity corrections for antenna gain characteristics included. The antenna gains employed for this purpose are presented in Table 3 and resulted from an interpolation of percent gain vs deviation from boresight to the desired bore sight deviation angles. This was accomplished for each of the seven bore sight directions. The present gain for each deviation angle was

then averaged over the seven bore sight directions to obtain mean values for each channel..

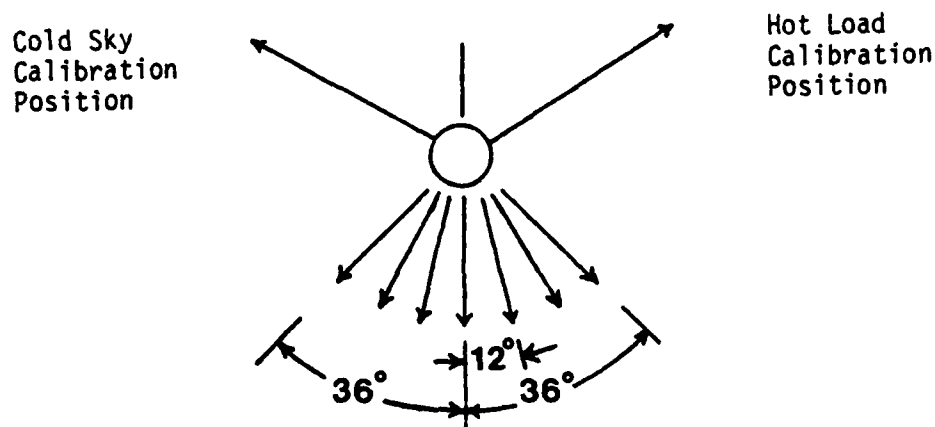


Figure 1. SSM/T Scan Geometry.

Source: Riogone and Stogryn (1977)

Table 1. Channel Parameter Design Specifications

Channel	Polarization	Frequency (GHz)	Bandwidth (MHz)	NETD ($^{\circ}\text{K}$)
1	Principally Horizontal	50.5	400	0.6
2		53.2	400	0.4
3		54.35	400	0.4
4		54.9	400	0.4
5	Orthogonal to Channels 1-4	58.4	115	0.5
6		58.825	400	0.4
7		59.4	250	0.4

Source: Riogone and Stogryn (1977)

Table 2. Scan Parameters

Scan Type	Cross-Track Nadir
Cross-Track Positions	7
Calibration Positions	2-Cold Space and 300°K
Instantaneous Field of View	14°
Total Cross-Track Scan	36°
Total Scan Period	32 Seconds
Integration Time (Cross-track and Calibration Positions)	2.7 Seconds
Sync Mode	Auto Mode of On-Sync

Source: Riogone and Stogryn (1977)

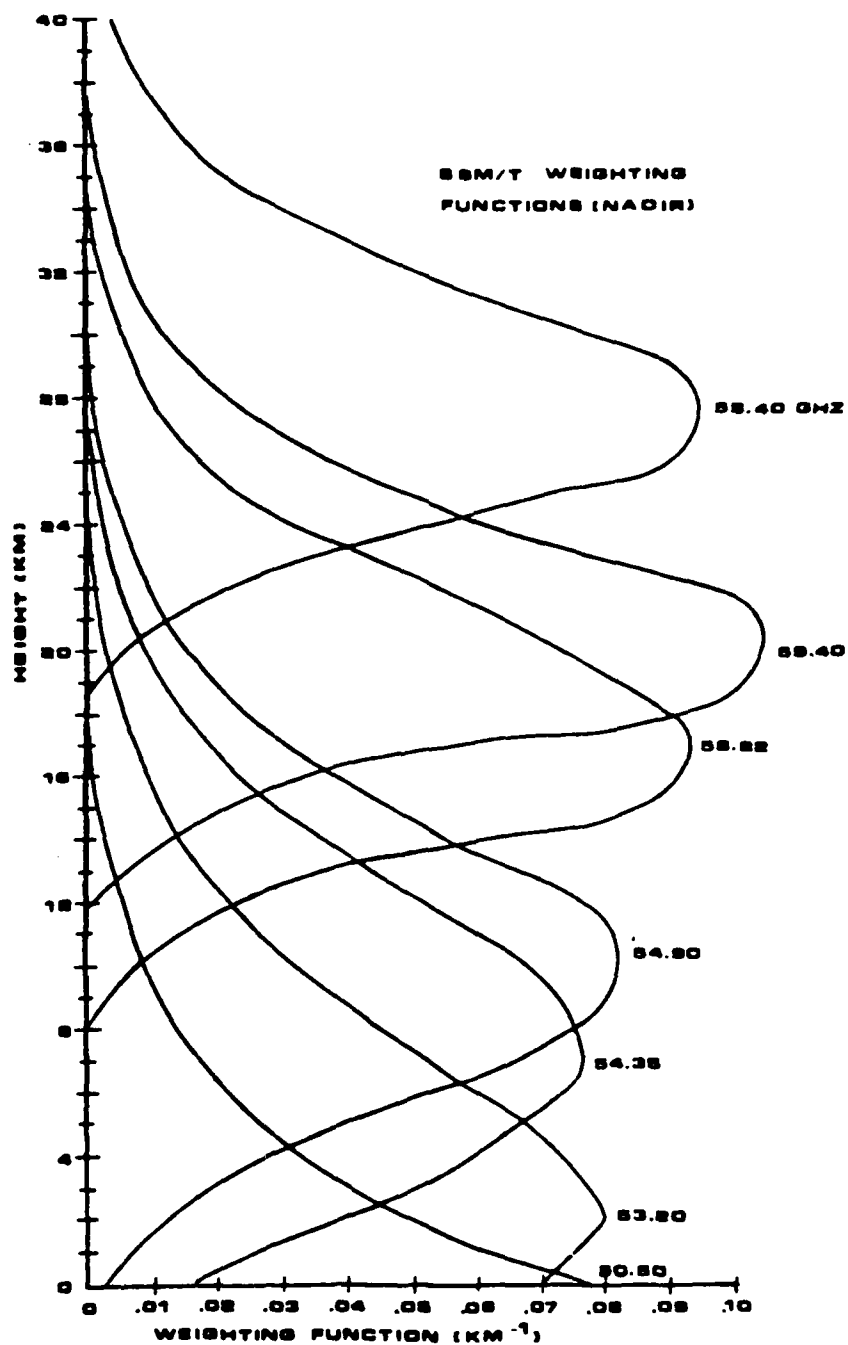


Figure 2. SSM/T Weighting Functions (Nadir), Antenna Gain Characteristics included, $\epsilon=.97$.

Table 3. Percent Gains Averaged Over Bore Sight Angles

0°	Channel Frequencies (GHz)						
	50.50	53.20	54.35	54.90	58.40	58.82	59.40
0.	99.357	99.675	99.675	99.675	100.000	99.727	99.350
1.	97.583	97.901	97.901	97.901	97.360	96.987	96.473
2.	93.819	93.877	94.217	94.379	91.545	91.577	91.622
3.	88.301	88.095	88.772	89.096	83.173	83.012	82.790
4.	80.706	79.643	80.360	80.702	72.161	71.892	71.519
5.	70.741	68.905	69.138	69.249	59.177	58.694	58.028
6.	59.742	56.612	56.192	55.991	46.061	45.185	43.976
7.	48.659	43.934	43.228	42.890	34.283	33.306	31.956
8.	37.555	32.230	31.664	31.393	24.283	23.550	22.536
9.	27.325	22.201	21.861	21.698	15.793	15.246	14.490
10.	18.778	13.867	13.930	13.961	8.990	9.082	9.209
11.	12.523	6.893	6.926	6.942	5.466	5.266	4.990
12.	7.698	4.729	4.694	4.678	2.764	2.936	3.173
13.	5.189	3.129	2.899	2.789	1.691	1.613	1.505
14.	3.539	1.871	1.495	1.316	.899	.846	.773
15.	2.212	1.106	.725	.543	.441	.421	.393
16.	1.353	.601	.335	.208	.311	.288	.255
17.	.834	.282	.220	.190	.229	.216	.199
18.	.464	.247	.230	.223	.166	.163	.158
19.	.267	.249	.225	.213	.130	.146	.167
20.	.194	.230	.197	.182	.096	.125	.166
21.	.157	.192	.164	.150	.064	.096	.141
22.	.123	.163	.140	.128	.048	.077	.118
23.	.093	.137	.118	.108	.051	.070	.096
24.	.070	.113	.098	.091	.049	.062	.080
25.	.048	.093	.085	.081	.043	.055	.072
26.	.034	.073	.072	.071	.037	.049	.065
27.	.038	.058	.061	.063	.033	.043	.058
28.	.042	.048	.052	.054	.030	.039	.051
29.	.039	.039	.044	.046	.028	.034	.042

Table 3. (Continued)

0°	Channel Frequencies (GHz)						
	50.50	53.20	54.35	54.90	58.40	58.82	59.40
30.	.032	.029	.035	.038	.025	.028	.032
31.	.025	.025	.029	.030	.024	.025	.025
32.	.019	.022	.025	.026	.023	.021	.017
33.	.013	.024	.027	.029	.022	.018	.013
34.	.011	.026	.031	.033	.022	.018	.012
35.	.010	.027	.033	.035	.021	.017	.012
36.	.011	.027	.030	.032	.020	.017	.013
37.	.012	.025	.027	.028	.020	.017	.013
38.	.014	.024	.024	.024	.019	.017	.013
39.	.016	.021	.020	.019	.019	.016	.013
40.	.019	.019	.016	.015	.018	.016	.015
41.	.021	.018	.014	.012	.017	.016	.016
42.	.021	.017	.012	.010	.016	.016	.017
43.	.021	.018	.011	.008	.015	.016	.018
44.	.021	.018	.010	.006	.014	.016	.019
45.	.020	.017	.009	.005	.013	.016	.020
46.	.020	.015	.008	.005	.013	.016	.021
47.	.019	.014	.008	.006	.012	.016	.021
48.	.018	.013	.009	.007	.012	.016	.022
49.	.017	.012	.009	.008	.012	.016	.022
50.	.016	.012	.010	.009	.011	.016	.022
51.	.016	.011	.011	.011	.011	.015	.021
52.	.015	.010	.011	.011	.010	.014	.021
53.	.015	.009	.011	.012	.009	.013	.019
54.	.014	.009	.011	.012	.009	.012	.018
55.	.014	.008	.011	.012	.008	.011	.016
56.	.013	.008	.011	.012	.007	.010	.014
57.	.013	.007	.010	.012	.007	.009	.012
58.	.012	.007	.010	.011	.006	.008	.011
59.	.011	.007	.009	.010	.006	.007	.009

Table 3. (Continued)

0°	Channel Frequencies (GHz)						
	50.05	53.20	54.35	54.90	58.40	58.82	59.40
60.	.010	.006	.008	.009	.005	.006	.008
61.	.010	.009	.009	.009	.005	.006	.007
62.	.009	.011	.009	.008	.004	.005	.006
63.	.008	.014	.009	.007	.004	.004	.005

CHAPTER 3

OPTICAL PARAMETERS FOR SSM/T CHANNELS

3.1 Mie Theory

The application of Mie scattering theory enables calculation of optical parameters for assumed spherical particles; given the complex index of refraction, wave length of radiation to be scattered and particle size density distribution. The Mie program used for these calculations is a modification for Univac computers of the program by Liou and Hansen (1971). The output of the Mie computations include the coefficients of the Legendre polynomial approximation to the phase function, the extinction coefficient (Km^{-1}) and the single scattering albedo. Note that the extinction coefficient and single scattering albedo determined here include scattering and absorption by the particles as the only mechanisms for extinction. These values are modified to include absorption by the gaseous atmosphere within the cloud prior to their use in the solution of the radiative transfer equation.

3.2 Indices of Refraction

The complex indices of refraction for pure liquid water at temperatures of $+10^{\circ}$ and -10° C have been determined by Savage (1976) for several different frequencies. These values (Table 4) are based on a least squares fit to the data of Saxton and Lane (1962) given by Hollinger (1973). The complex indices of refraction for the SSM/T channels (Table 5) were obtained from Table 4 by linear interpolation

Table 4. Refractive Index $m=m_r-im_i$ of Pure Liquid Water

Frequency (Ghz)	T=10°C		T=0°C		T=-10°C	
	m_r	m_i	m_r	m_i	m_r	m_i
19.35	5.87	2.96	5.20	2.94	4.64	2.81
37.00	4.32	2.60	3.83	2.37	3.46	2.12
50.30	3.76	2.29	3.37	2.03	3.08	1.78
89.50	3.00	1.67	2.76	1.42	2.60	1.20
100.00	2.89	1.56	2.68	1.31	2.54	1.10
118.00	2.75	1.39	2.58	1.15	2.46	0.96
130.00	2.68	1.30	2.53	1.07	2.43	0.89
183.00	2.49	1.00	2.39	0.81	2.33	0.66
231.00	2.40	0.82	2.33	0.66	2.29	0.53

After Savage (1976)

Table 5. Refractive Index of Pure Liquid Water (SSM/T)

	Channel Frequencies (GHz)						
	50.50	53.20	54.35	54.90	58.40	58.82	59.40
m_r	3.37	3.32	3.31	3.30	3.24	3.24	3.23
m_i	2.03	1.98	1.97	1.96	1.90	1.90	1.89

in frequency. For the purpose of this study the values for 0°C are used throughout. It is important to note, however, that after the Block 5D satellite flys, greater care may be necessary to insure that the indices of refraction are compatible with atmospheric temperatures at cloud levels if observed brightness temperatures are to be matched by theoretical calculations.

3.3 Drop Size Distributions

Once the absorption and scattering efficiencies for single particles have been determined by Mie theory in terms of effective cross sectional area, the efficiencies for a distribution of particles can be determined by integrating over the distribution. This area per volume relationship then has dimensions of inverse length and is described as the absorption (or scattering, or extinction) coefficient. The drop size distributions used for this study are necessarily numerical models. Two models have been chosen to represent nonprecipitating and precipitating clouds, respectively. Deirmendjian's L-Model cloud (Deirmendjian, 1969) drop size distribution is used for the nonprecipitating case, that is:

$$N(r) = ar^{\alpha} \exp(-br^{\delta}), \quad (3-1)$$

where r is the drop radius in mm. By varying the constants this model can be made to represent a variety of cloud types. For this study, $a=4.9757 \times 10^7$, $\alpha=2$, $b=15.1186$, and $\delta=.5$. For the precipitating case, a theoretical drop size distribution based on rainfall rate is used (Marshall and Palmer, 1948). The distribution is expressed by:

$$N(r) = 0.08 \exp(-2r\delta) \quad (3-2)$$

where $\delta=41R^{-.21}$ and R denotes rainfall rate (mm/hr.). This exponential behavior of drop size distribution has been experimentally verified by Gunn and Marshall (1958) and Sekhon and Srivastava (1970).

3.4 Parameter Values

The Legendre polynomial phase function coefficients, extinction coefficients and single scattering albedos calculated for each SSM/T channel from Mie theory are tabulated in Tables 6-16. Since the

extinction coefficient input to the radiative transfer program must be in units of (Km^{-1}) the final values ouput by the Mie program have been multiplied by the proper constant to obtain these units.

Table 6. Optical Parameters (Deirmendjian L-Model)

Freq(GHz)	$\bar{\omega}_0$	$\bar{\omega}_1$	$\bar{\omega}_2$	$\bar{\omega}_3$	$\bar{\omega}_4$	$\bar{\omega}_5$
	$\bar{\omega}_6$	$\bar{\omega}_7$	$\bar{\omega}_8$	$\bar{\omega}_9$	$\bar{\omega}_{10}$	$\bar{\omega}_{11}$
	$\bar{\omega}_{12}$	$\bar{\omega}_{13}$	$\bar{\omega}_{14}$	$\bar{\omega}_{15}$	β_{ext}	$\bar{\omega}_v$
50.50 GHz						
.10000000E+1	.33071515E+0	.49360468E+0	.11251515E+0	-.75388403E-2	-.64620544E-2	
-.61193658E-1	-.19706414E-1	-.72342400E-1	-.21862288E-1	-.73393241E-1	-.21065428E-1	
-.56718646E-1	-.18075541E-1	-.53308599E-1	-.13297797E-1	.19639240E+0	.371442	
53.20 GHz						
.10000000E+1	.36502548E+0	.50176195E+0	.12244376E+0	-.16683441E-2	-.59117595E-2	
-.60940647E-1	-.21526171E-1	-.72936066E-1	-.24082668E-1	-.74087993E-1	-.23228360E-1	
-.67363482E-1	-.19934813E-1	-.53830418E-1	-.14667078E-1	.21121971E+0	.378722	
54.35 GHz						
.10000000E+1	.37639293E+0	.50474406E+0	.12667598E+0	.92690317E-3	-.54816648E-2	
-.60773288E-1	-.22136718E-1	-.73163086E-1	-.24870594E-1	-.74365129E-1	-.24001107E-1	
-.67622238E-1	-.20600170E-1	-.54040190E-1	-.15157736E-1	.21741939E+0	.382306	
54.90 GHz						
.10000000E+1	.38338237E+0	.50662057E+0	.12879932E+0	.22010716E-2	-.53178290E-2	
-.60704117E-1	-.22500922E-1	-.73293393E-1	-.25328362E-1	-.74521266E-1	-.24448971E-1	
-.6776713E-1	-.20985495E-1	-.54157977E-1	-.15441639E-1	.22034972E+0	.383564	
58.40 GHz						
.10000000E+1	.42759183E+0	.51955854E+0	.14307608E+0	.10864534E-1	-.39435839E-2	
-.60144363E-1	-.24772093E-1	-.74167010E-1	-.28268136E-1	-.75591876E-1	-.27337488E-1	
-.68768864E-1	-.23473136E-1	-.54969336E-1	-.17275603E-1	.23852110E+0	.391119	
58.82 GHz						
.10000000E+1	.43064151E+0	.52059478E+0	.14467422E+0	.11900079E-1	-.36744970E-2	
-.60041932E-1	-.24929679E-1	-.74243871E-1	-.28504663E-1	-.75695095E-1	-.27573876E-1	
-.68866560E-1	-.23677469E-1	-.55048812E-1	-.17426715E-1	.24066970E+0	.392445	
59.40 GHz						
.10000000E+1	.43805500E+0	.52296755E+0	.14716554E+0	.13424878E-1	-.33915394E-2	
-.59927715E-1	-.25301872E-1	-.74397610E-1	-.29002240E-1	-.75888122E-1	-.28065275E-1	
-.69047813E-1	-.24101133E-1	-.55195863E-1	-.17739194E-1	.24356932E+0	.393526	

Table 7. Optical Parameters (Marshall-Palmer 1mm/hr)

Freq (GHz)	$\bar{\omega}_1$	$\bar{\omega}_2$	$\bar{\omega}_3$	$\bar{\omega}_4$	$\bar{\omega}_5$
$\bar{\omega}_0$					
50.50GHz					
.1000000E+1	.19833052E+0	.47688411E+0	.55118323E-1	-.39233125E-1	-.87157051E-2
-.62096694E-1	-.11531642E-1	-.70222380E-1	-.12313806E-1	-.71009004E-1	-.11824920E-1
-.64517421E-1	-.10137258E-1	-.51524593E-1	-.74482281E-2	.84232338E-1	.292315
53.20GHz					
.1000000E+1	.22402792E+0	.47839620E+0	.59819801E-1	-.37492504E-1	-.95918234E-2
-.62194212E-1	-.12922219E-1	-.70374822E-1	-.13802233E-1	-.71164137E-1	-.13254064E-1
-.64659236E-1	-.11362062E-1	-.51639036E-1	-.83475256E-1	.92745402E-1	.304235
54.35GHz					
.1000000E+1	.23205810E+0	.47878575E+0	.61910084E-1	-.36678740E-1	-.98396532E-2
-.62224228E-1	-.13385122E-1	-.70430895E-1	-.14298761E-1	-.71221342E-1	-.13730905E-1
-.64711583E-1	-.11770879E-1	-.51681400E-1	-.86479728E-1	.96396855E-1	.309626
54.90GHz					
.1000000E+1	.23750060E+0	.47918551E+0	.62929877E-1	-.36273642E-1	-.10013095E-1
-.62247228E-1	-.13680903E+0	-.70468713E-1	-.14615722E-1	-.71259849E-1	-.14035253E-1
-.64746761E-1	-.12031728E-1	-.51709807E-1	-.88395184E-2	.98139872E-1	.311786
58.40GHz					
.1000000E+1	.27220688E+0	.48214605E+0	.69720240E-1	-.33448139E-1	-.11069380E-1
-.62405476E-1	-.15579415E-1	-.70740726E-1	-.16653212E-1	-.71537185E-1	-.15991775E-1
-.65000162E-1	-.13708748E-1	-.51914319E-1	-.10071212E-1	.10920593E+0	.324571
58.82GHz					
.1000000E+1	.27427582E+0	.48225550E+0	.70554734E-1	-.33082321E-1	-.11109789E-1
-.62412982E-1	-.15711972E-1	-.70762828E-1	-.16796611E-1	-.71559851E-1	-.16129550E-1
-.65020926E-1	-.13826951E-1	-.51931131E-1	-.10158213E-1	.11054591E+0	.326468
59.40GHz					
.1000000E+1	.28023853E+0	.48286078E+0	.71740599E-1	-.32564901E-1	-.11279653E-1
-.62442334E-1	-.16038949E-1	-.70815697E-1	-.17148129E-1	-.71613804E-1	-.16467157E-1
-.65070226E-1	-.14116323E-1	-.51970903E-1	-.10370743E-1	.11236057E+0	.328350

Table 8. Optical Parameters (Marshall-Palmer, 2mm/hr.)

Freq(GHz)	$\bar{\omega}_1$	$\bar{\omega}_2$	$\bar{\omega}_3$	$\bar{\omega}_4$	$\bar{\omega}_5$
$\bar{\omega}_0$					
$\bar{\omega}_6$					
$\bar{\omega}_{12}$					
50.50GHz					
.1000000E+1	.23305293E+0	.47669795E+0	.69520500E-1	-.33475318E-1	-.95957994E-2
-.62175845E-1	-.13776946E-1	-.70478158E-1	-.14730295E-1	-.71271311E-1	-.14146668E-1
-.64758072E-1	-.12129186E-1	-.51720168E-1	-.89139807E-2	.17904705E+0	.333189
53.20GHz					
.1000000E+1	.26325986E+0	.47933453E+0	.75807102E-1	-.30618404E-1	-.10409493E-1
-.62303234E-1	-.15445792E-1	-.70736236E-1	-.16526853E-1	-.71535191E-1	-.15872090E-1
-.64999268E-1	-.13608205E-1	-.51914898E-1	-.10000476E-1	.19526609E+0	.343557
54.35GHz					
.1000000E+1	.27304477E+0	.48016100E+0	.78578498E-1	-.29300388E-1	-.10608633E-1
-.62339426E-1	-.16019093E-1	-.70836625E-1	-.17147537E-1	-.71638278E-1	-.16468370E-1
-.65093569E-1	-.14119549E-1	-.51991134E-1	-.10376438E-1	.20213311E+0	.348307
54.90GHz					
.1000000E+1	.27938366E+0	.48085325E+0	.79948634E-1	-.28644508E-1	-.10758994E-1
-.62367953E-1	-.16371191E-1	-.70899995E-1	-.17527962E-1	-.71703261E-1	-.16833752E-1
-.65152969E-1	-.14432824E-1	-.52039092E-1	-.10606620E-1	.20538624E+0	.350154
58.40GHz					
.1000000E+1	.31965204E+0	.48595885E+0	.89119851E-1	-.24116337E-1	-.11591706E-1
-.62553437E-1	-.18625856E-1	-.71353265E-1	-.19972884E-1	-.72168952E-1	-.19182567E-1
-.65578578E-1	-.16446644E-1	-.52382578E-1	-.12086596E-1	.22574856E+0	.360992
58.82GHz					
.1000000E+1	.32229704E+0	.48625726E+0	.90221748E-1	-.23540332E-1	-.11595119E-1
-.62559037E-1	-.18795815E-1	-.71394044E-1	-.20160143E-1	-.72211288E-1	-.19362601E-1
-.65617340E-1	-.16601176E-1	-.52413899E-1	-.12200346E-1	.22818576E+0	.362670
59.40GHz					
.1000000E+1	.32915882E+0	.48728307E+0	.91830136E-1	-.22720526E-1	-.11714991E-1
-.62591200E-1	-.19181183E-1	-.71480898E-1	-.20579983E-1	-.72300772E-1	-.19766032E-1
-.65699129E-1	-.16947077E-1	-.52479871E-1	-.12454616E-1	.23146830E+0	.364242

Table 9. Optical Parameters (Marshall-Palmer 3mm/hr)

Freq (Ghz)	$\bar{\omega}_1$	$\bar{\omega}_2$	$\bar{\omega}_3$	$\bar{\omega}_4$	$\bar{\omega}_5$
$\bar{\omega}_0$					
$\bar{\omega}_6$					
$\bar{\omega}_{12}$					
50.50Ghz					
.10000000E+1	.25862318E+0	.47744717E+0	.79897807E-1	-.28883795E-1	-.99653228E-1
-.62224346E-1	-.15418045E-1	-.70739437E-1	-.16511622E-1	-.71540767E-1	-.15858597E-1
-.65005033E-1	-.13597997E-1	-.51920506E-1	-.99950262E-1	.27383706E+0	.355154
53.20Ghz					
.10000000E+1	.29162371E+0	.48117814E+0	.8782297E-1	-.24840494E-1	-.10646886E-1
-.62359262E-1	-.17264665E-1	-.71090662E-1	-.18513792E-1	-.71901868E-1	-.17782016E-1
-.65335110E-1	-.15247116E-1	-.52186991E-1	-.11206979E-1	.29677251E+0	.364537
54.35Ghz					
.10000000E+1	.30252529E+0	.48244693E+0	.90664385E-1	-.23128135E-1	-.10770838E-1
-.62392209E-1	-.17909504E-1	-.71230216E-1	-.19219201E-1	-.72046216E-1	-.18460047E-1
-.65467236E-1	-.15288707E-1	-.52293727E-1	-.11634725E-1	.30640090E+0	.368894
54.90Ghz					
.10000000E+1	.30941458E+0	.48341050E+0	.92299544E-1	-.22275960E-1	-.10883022E-1
-.62420361E-1	-.18297148E-1	-.71315535E-1	-.19642109E-1	-.72134340E-1	-.18866422E-1
-.65547707E-1	-.16177158E-1	-.52358718E-1	-.11890848E-1	.31094508E+0	.370550
58.40Ghz					
.10000000E+1	.35308196E+0	.49045007E+0	.10325306E+0	-.16426243E-1	-.11419156E-1
-.62589478E-1	-.20771828E-1	-.71920656E-1	-.22359124E-1	-.72761442E-1	-.21478142E-1
-.66121005E-1	-.18416918E-1	-.52821356E-1	-.13537574E-1	.33915074E+0	.380231
58.82Ghz					
.10000000E+1	.35609849E+0	.49093359E+0	.10455210E+0	-.15689422E-1	-.11379821E-1
-.62588423E-1	-.20965118E-1	-.71977381E-1	-.22576647E-1	-.72821073E-1	-.21687536E-1
-.66175624E-1	-.18596657E-1	-.52865535E-1	-.13669973E-1	.34249930E+0	.381782
59.40Ghz					
.10000000E+1	.36350373E+0	.49232587E+0	.10647667E+0	-.14636938E-1	-.11438722E-1
-.62614921E-1	-.21385745E-1	-.72091952E-1	-.23042074E-1	-.72940414E-1	-.22135110E-1
-.66284733E-1	-.18980559E-1	-.52953556E-1	-.13952286E-1	.34700110E+0	.383173

Table 10. Optical Parameters (Marshall-Palmer 4mm/hr)

Freq(GHz)	$\bar{\omega}_1$	$\bar{\omega}_2$	$\bar{\omega}_3$	$\bar{\omega}_4$	$\bar{\omega}_5$
$\bar{\omega}_0$					
50.50GHz					
.1000000E+1	.27936264E+0	.47868582E+0	.88328239E-1	-.24241288E-1	-.10081960E-1
-.62247414E-1	-.16744915E-1	-.70998671E-1	-.17965453E-1	-.71809772E-1	-.17256226E-1
-.65251498E-1	-.14797347E-1	-.52120194E-1	-.10878014E-1	.36732478E+0	.369816
53.20GHz					
.1000000E+1	.31439899E+0	.48345105E+0	.96808990E-1	-.19747665E-1	-.10603425E-1
-.62374929E-1	-.18722155E-1	-.71433327E-1	-.20126367E-1	-.72259238E-1	-.19332913E-1
-.65662419E-1	-.16578150E-1	-.52451921E-1	-.12107055E-1	.39625288E+0	.378498
54.35GHz					
.1000000E+1	.32612371E+0	.48514269E+0	.10050889E+0	-.17703004E-1	-.10647098E-1
-.62398036E-1	-.19418578E-1	-.71607836E-1	-.20897355E-1	-.72441265E-1	-.20074386E-1
-.65928970E-1	-.17214275E-1	-.52586506E-1	-.12655095E-1	.40832036E+0	.382578
54.90GHz					
.1000000E+1	.33341119E+0	.48635588E+0	.10236397E+0	-.16685712E-1	-.10717014E-1
-.62422105E-1	-.19831740E-1	-.71712340E-1	-.21352967E-1	-.72549975E-1	-.20512442E-1
-.65928373E-1	-.17589948E-1	-.52666753E-1	-.12931337E-1	.41400230E+0	.384100
58.40GHz					
.1000000E+1	.37952617E+0	.49514276E+0	.11479302E+0	-.97308619E-2	-.10933021E-1
-.62549152E-1	-.22462198E-1	-.72440498E-1	-.24279620E-1	-.73319786E-1	-.23327733E-1
-.66632457E-1	-.20004832E-1	-.53234964E-1	-.14707537E-1	.44906141E+0	.392979
58.82GHz					
.1000000E+1	.38281677E+0	.49579889E+0	.11625385E+0	-.88608076E-2	-.10849801E-1
-.62538725E-1	-.22671747E-1	-.72518961E-1	-.24520767E-1	-.73394912E-1	-.23560197E-1
-.66701285E-1	-.20204411E-1	-.53290565E-1	-.14854617E-1	.45319756E+0	.394443
59.40GHz					
.1000000E+1	.39061003E+0	.49751566E+0	.11843982E+0	-.76143673E-2	-.10845311E-1
-.62554641E-1	-.23116588E-1	-.72657073E-1	-.25021294E-1	-.73540332E-1	-.24041975E-1
-.66834305E-1	-.20617730E-1	-.53397930E-1	-.15158714E-1	.45875429E+0	.395710

Table 11. Optical Parameters (Marshall-Palmer 5mm/hr)

Freq (Ghz)	$\bar{\omega}_1$	$\bar{\omega}_2$	$\bar{\omega}_3$	$\bar{\omega}_4$	$\bar{\omega}_5$
$\bar{\omega}_0$					
$\bar{\omega}_6$					
$\bar{\omega}_{12}$					
50.50GHz					
.1000000E+1	.29701037E+0	.48021003E+0	.95563178E-1	-.20293266E-1	-.10044780E-1
-.62248691E-1	-.17870954E-1	-.71252878E-1	-.19211714E-1	-.72075326E-1	-.18454867E-1
-.65494738E-1	-.15826063E-1	-.52317221E-1	-.11635461E-1	.45922777E+0	.380662
53.20GHz					
.1000000E+1	.33364779E+0	.48594835E+0	.10490631E+0	-.15141100E-1	-.10397982E-1
-.62358333E-1	-.19949749E-1	-.71763088E-1	-.21503093E-1	-.72606076E-1	-.20657868E-1
-.65520102E-1	-.17715456E-1	-.52709038E-1	-.13024754E-1	.49359412E+0	.388807
54.35GHz					
.1000000E+1	.34602374E+0	.48803910E+0	.10896940E+0	-.12807568E-1	-.10356365E-1
-.62367490E-1	-.20686403E-1	-.71969109E-1	-.22328454E-1	-.72822629E-1	-.21452143E-1
-.66178294E-1	-.18396925E-1	-.52869161E-1	-.13526324E-1	.50785787E+0	.392676
54.90GHz					
.1000000E+1	.35362231E+0	.49848256E+0	.11101520E+0	-.11646018E-1	-.10382346E-1
-.62384982E-1	-.21119020E-1	-.72090750E-1	-.22811007E-1	-.72950132E-1	-.21916366E-1
-.66294909E-1	-.18795166E-1	-.52963325E-1	-.13819264E-1	.51456302E+0	.394098
58.40GHz					
.1000000E+1	.40164200E+0	.49986409E+0	.12472816E+0	-.37268698E-2	-.10271454E-1
-.62451675E-1	-.23865646E-1	-.72942269E-1	-.25910449E-1	-.73848994E-1	-.24900478E-1
-.67117426E-1	-.21355418E-1	-.53627074E-1	-.15702963E-1	.55574798E+0	.402370
58.82GHz					
.1000000E+1	.40514901E+0	.50068025E+0	.12632884E+0	-.27413713E-2	-.10144515E-1
-.62430076E-1	-.24087027E-1	-.73024837E-1	-.26171168E-1	-.73938141E-1	-.25152175E-1
-.67199188E-1	-.21571546E-1	-.53693186E-1	-.15862288E-1	.56068187E+0	.403769
59.40GHz					
.1000000E+1	.41324203E+0	.50268880E+0	.12874159E+0	-.13263080E-2	-.10076593E-1
-.62432216E-1	-.24549362E-1	-.73183344E-1	-.26700501E-1	-.74108899E-1	-.25662317E-1
-.67353649E-1	-.22009285E-1	-.53817836E-1	-.16184493E-1	.56707465E+0	.404943

Table 12. Optical Parameters (Marshall-Palmer 10mm/hr)

Freq (Ghz)	$\bar{\omega}_1$	$\bar{\omega}_2$	$\bar{\omega}_3$	$\bar{\omega}_4$	$\bar{\omega}_5$
$\bar{\omega}_0$					
50.50Ghz					
.10000000E+1	.36093848E+0	.48951757E+0	.12262584E+0	-.41402253E-2	-.87863093E-2
-.62023475E-1	-.21908425E-1	-.72427155E-1	-.23817222E-1	-.73326414E-1	-.22891432E-1
-.66641428E-1	-.19634845E-1	-.53245206E-1	-.14441571E-1	.89594238E+0	.411507
53.20Ghz					
.10000000E+1	.40258453E+0	.49938498E+0	.13527074E+0	.35405875E-2	-.82581204E-2
-.61953387E-1	-.24281849E-1	-.73234870E-1	-.26559573E-1	-.74193661E-1	-.25536095E-1
-.67435929E-1	-.21904511E-1	-.53886577E-1	-.16112319E-1	.95218622E+0	.418062
54.35Ghz					
.10000000E+1	.41701050E+0	.50317153E+0	.14071610E+0	.69763924E-2	-.77908956E-2
-.61854523E-1	-.25128965E-1	-.73562758E-1	-.27573228E-1	-.74552777E-1	-.26515943E-1
-.67765408E-1	-.22746010E-1	-.54152811E-1	-.16732326E-1	.97515409E+0	.421319
54.90Ghz					
.10000000E+1	.42556904E+0	.50556084E+0	.14349197E+0	.86890517E-2	-.75975237E-2
-.61818749E-1	-.25613949E-1	-.73749411E-1	-.28148646E-1	-.74756449E-1	-.27072021E-1
-.67952174E-1	-.23223385E-1	-.54303589E-1	-.17083881E-1	.98590729E+0	.422445
58.40Ghz					
.10000000E+1	.47941101E+0	.52235422E+0	.16208856E+0	.20282942E-1	-.59096163E-2
-.61453676E-1	-.28648382E-1	-.75027062E-1	-.31840407E-1	-.76170676E-1	-.30647488E-1
-.69250819E-1	-.26293969E-1	-.55352102E-1	-.19346159E-1	.10510474E+1	.428964
58.82Ghz					
.10000000E+1	.48359282E+0	.52382556E+0	.16421848E+0	.21703873E-1	-.55778436E-2
-.61362985E-1	-.28895100E-1	-.75153129E-1	-.32168380E-1	-.76316263E-1	-.30967215E-1
-.69385021E-1	-.26568938E-1	-.55460665E-1	-.19549150E-1	.10585614E+1	.430178
59.40Ghz					
.10000000E+1	.49258928E+0	.52697968E+0	.16749501E+0	.23761808E-1	-.52100210E-2
-.61273778E-1	-.29394957E-1	-.75384309E-1	-.32796124E-1	-.76576783E-1	-.31576998E-1
-.69624639E-1	-.27092870E-1	-.55654148E-1	-.19935314E-1	.10686664E+1	.431085

Table 13. Optical Parameters (Marshall-Palmer 15mm/hr)

Freq(GHz)	$\bar{\omega}_1$	$\bar{\omega}_2$	$\bar{\omega}_3$	$\bar{\omega}_4$	$\bar{\omega}_5$
$\bar{\omega}_0$					
$\bar{\omega}_6$					
$\bar{\omega}_{12}$					
50.50GHz					
.1000000E+1	.40489974E+0	.49945961E+0	.14234551E+0	.86064041E-2	-.67925486E-2
-.61550264E-1	-.24612721E-1	-.73452160E-1	-.27083996E-1	-.74456659E-1	-.26050576E-1
-.67679281E-1	-.22348698E-1	-.54084738E-1	-.16442662E-1	.13016306E+1	.427672
53.20GHz					
.10000000E+1	.44941841E+0	.51260638E+0	.15744676E+0	.18158680E-1	-.54152315E-2
-.61228033E-1	-.27113496E-1	-.74472934E-1	-.30122669E-1	-.75588129E-1	-.28993056E-1
-.68718405E-1	-.24875565E-1	-.54923891E-1	-.18304254E-1	.13745169E+1	.433375
54.35GHz					
.10000000E+1	.46502350E+0	.51773404E+0	.16391647E+0	.22405226E-1	-.45496123E-2
-.60992755E-1	-.2799760E-1	-.74885064E-1	-.31259461E-1	-.76058520E-1	-.30098638E-1
-.69151511E-1	-.25825809E-1	-.55273948E-1	-.19005093E-1	.14039892E+1	.436308
54.90GHz					
.10000000E+1	.47412169E+0	.52084973E+0	.16723198E+0	.24525361E-1	-.41537489E-2
-.60888758E-1	-.28501636E-1	-.75115838E-1	-.31895147E-1	-.76320671E-1	-.30716643E-1
-.69392801E-1	-.26356845E-1	-.55468810E-1	-.19396531E-1	.14177649E+1	.437277
58.40GHz					
.10000000E+1	.53119208E+0	.54246361E+0	.18944828E+0	.38836538E-1	-.10219920E-2
-.5998916E-1	-.31595389E-1	-.76670204E-1	-.35969580E-1	-.78124808E-1	-.34693194E-1
-.71057164E-1	-.29775847E-1	-.56813578E-1	-.21918156E-1	.15005644E+1	.442872
58.82GHz					
.10000000E+1	.53575518E+0	.54443285E+0	.19196726E+0	.40574308E-1	-.50714008E-3
-.59832359E-1	-.31841726E-1	-.76822736E-1	-.36340519E-1	-.78312949E-1	-.35059194E-1
-.71231725E-1	-.30091143E-1	-.56954878E-1	-.22151202E-1	.15100086E+1	.443992
59.40GHz					
.10000000E+1	.54524228E+0	.54842635E+0	.19588108E+0	.43107757E-1	.12957861E-3
-.59637668E-1	-.32340639E-1	-.77098336E-1	-.37031008E-1	-.78641636E-1	-.35736896E-1
-.71535870E-1	-.30674074E-1	-.57200689E-1	-.22581343E-1	.15227365E+1	.444759

Table 14. Optical Parameters (Marshall-Palmer 20mm/hr)

Freq(GHz)	$\bar{\omega}_1$	$\bar{\omega}_2$	$\bar{\omega}_3$	$\bar{\omega}_4$	$\bar{\omega}_5$
$\bar{\omega}_0$					
$\bar{\omega}_6$					
$\bar{\omega}_{12}$				$\bar{\omega}_{10}$	$\bar{\omega}_v$
50.50GHz				β_{ext}	
.1000000E+1	.4390376E+0	.5091979E+0	.1584532E+0	.1942762E-1	-.45405659E-2
-.6092971E-1	-.2664222E-1	-.7435778E-1	-.2968416E-1	-.7548956E-1	-.28577161E-1
-.6863022E-1	-.2452049E-1	-.5485405E-1	-.1804520E-1	.1683856E+1	.438371
53.20GHz					
.1000000E+1	.4855249E+0	.5250797E+0	.1755023E+0	.3051787E-1	-.2365143E-2
-.6032440E-1	-.2919057E-1	-.7553941E-1	-.3294621E-1	-.7684201E-1	-.3175146E-1
-.6987596E-1	-.2724840E-1	-.5586047E-1	-.2005642E-1	.1770370E+1	.443509
54.35GHz					
.1000000E+1	.5019373E+0	.5313203E+0	.1828961E+0	.3542675E-1	-.1128633E-2
-.5994329E-1	-.3008309E-1	-.7601282E-1	-.3417522E-1	-.7740473E-1	-.3295510E-1
-.7039620E-1	-.2828403E-1	-.5628116E-1	-.2082079E-1	.1805103E+1	.446229
54.90GHz					
.1000000E+1	.5113998E+0	.5350301E+0	.1866570E+0	.3788171E-1	-.5443931E-3
-.5976543E-1	-.3058571E-1	-.7627550E-1	-.3485600E-1	-.7771503E-1	-.3362146E-1
-.7068300E-1	-.2885720E-1	-.5651297E-1	-.2124361E-1	.1821324E+1	.447094
58.40GHz					
.1000000E+1	.5706262E+0	.5605348E+0	.2118422E+0	.5442927E-1	.3909717E-2
-.5832193E-1	-.3363288E-1	-.7801959E-1	-.3921243E-1	-.7983692E-1	-.3791091E-1
-.7265084E-1	-.3255002E-1	-.5810415E-1	-.2396966E-1	.1918294E+1	.452083
58.82GHz					
.1000000E+1	.5754464E+0	.5629068E+0	.2146796E+0	.5642620E-1	.4589800E-2
-.5807791E-1	-.3386653E-1	-.7818871E-1	-.3961449E-1	-.8005964E-1	-.3831300E-1
-.7285901E-1	-.3289709E-1	-.5827286E-1	-.2422648E-1	.1929260E+1	.453141
59.40GHz					
.1000000E+1	.5852563E+0	.5675676E+0	.2191144E+0	.5935155E-1	.5470643E-2
-.5777434E-1	-.3434708E-1	-.7849279E-1	-.4035044E-1	-.8044310E-1	-.3904328E-1
-.7321623E-1	-.3352658E-1	-.5856188E-1	-.2469146E-1	.1944073E+1	.453817

Table 15. Optical Parameters (Marshall-Palmer 25mm/hr)

Freq (Ghz)	$\bar{\omega}_0$	$\bar{\omega}_1$	$\bar{\omega}_2$	$\bar{\omega}_3$	$\bar{\omega}_4$	$\bar{\omega}_5$
$\bar{\omega}_6$	$\bar{\omega}_7$	$\bar{\omega}_8$	$\bar{\omega}_9$	$\bar{\omega}_{10}$	$\bar{\omega}_{11}$	
$\bar{\omega}_{12}$	$\bar{\omega}_{13}$	$\bar{\omega}_{14}$	$\bar{\omega}_{15}$	β_{ext}	$\bar{\omega}_v$	
50.50Ghz						
.1000000E+1	.46717341E+0	.51855401E+0	.17232806E+0	.28967801E-1		-.21834488E-2
-.60213211E-1	-.28249534E-1	-.75167057E-1	-.31870951E-1	-.76444522E-1		-.30713691E-1
-.69512096E-1	-.26358383E-1	-.55567630E-1	-.19402249E-1	.20475379E+1		.446257
53.20Ghz						
.10000000E+1	.51512995E+0	.53678951E+0	.19121456E+0	.41386600E-1		.74454173E-3
-.59310646E-1	-.30798992E-1	-.76473803E-1	-.35312376E-1	-.77987951E-1		-.34080889E-1
-.70938488E-1	-.29254492E-1	-.56720548E-1	-.21538707E-1	.21456670E+1		.450980
54.35Ghz						
.10000000E+1	.53214434E+0	.54398351E+0	.19925572E+0	.46867901E-1		.23248313E-2
-.58779234E-1	-.31677175E-1	-.76992487E-1	-.36614429E-1	-.78630161E-1		-.35365866E-1
-.71534858E-1	-.30361208E-1	-.57203110E-1	-.22356254E-1	.21848400E+1		.453545
54.90Ghz						
.10000000E+1	.54187524E+0	.54819744E+0	.20340130E+0	.49612777E-1		.30848575E-2
-.58525542E-1	-.32170743E-1	-.77278504E-1	-.37330867E-1	-.78981650E-1		-.36072509E-1
-.71861179E-1	-.30969705E-1	-.57467045E-1	-.22805463E-1	.22031279E+1		.454335
58.40Ghz						
.10000000E+1	.60267618E+0	.57697304E+0	.23114114E+0	.68094563E-1		.87656564E-2
-.56522240E-1	-.35111644E-1	-.79154474E-1	-.41907684E-1	-.81372392E-1		-.40622032E-1
-.74090999E-1	-.34892315E-1	-.59271781E-1	-.25703557E-1	.23119910E+1		.458881
58.82Ghz						
.10000000E+1	.60768566E+0	.57968392E+0	.23425180E+0	.70314457E-1		.95974271E-2
-.56201517E-1	-.35325828E-1	-.79333503E-1	-.4233479E-1	-.81624045E-1		-.41053989E-1
-.74328186E-1	-.35266001E-1	-.59464233E-1	-.25980347E-1	.23242168E+1		.459895
59.40Ghz						
.10000000E+1	.61772795E+0	.58489953E+0	.23913298E+0	.73579252E-1		.10703176E-1
-.55789220E-1	-.35778189E-1	-.79655550E-1	-.43104248E-1	-.82053374E-1		-.41828149E-1
-.74730993E-1	-.35934602E-1	-.59790541E-1	-.26474721E-1	.23407661E+1		.460503

Table 16. Optical Parameters (Marshall-Palmer 30mm/hr)

Freq (Ghz)	$\bar{\omega}_1$	$\bar{\omega}_2$	$\bar{\omega}_3$	$\bar{\omega}_4$	$\bar{\omega}_5$
$\bar{\omega}_0$					
$\bar{\omega}_6$					
$\bar{\omega}_{12}$					
50.50GHz					
.1000000E+1	.49121131E+0	.52749945E+0	.18465455E+0	.37577904E-1	.21290313E-3
-.59429845E-1	-.29563076E-1	-.75897299E-1	-.33771160E-1	-.7733382E-1	-.32581278E-1
-.70337569E-1	-.27966255E-1	-.56235893E-1	-.20590112E-1	.23960058E+1	.452447
53.20GHz					
.10000000E+1	.54032236E+0	.54780426E+0	.20510323E+0	.51180242E-1	.38509139E-2
-.58223647E-1	-.32082087E-1	-.77302182E-1	-.37361464E-1	-.79047595E-1	-.36114894E-1
-.71925554E-1	-.31008134E-1	-.57520069E-1	-.22835439E-1	.25042903E+1	.456847
54.35GHz					
.10000000E+1	.55780879E+0	.55583315E+0	.21379108E+0	.57168584E-1	.57554127E-2
-.57541798E-1	-.32934138E-1	-.77854825E-1	-.38723578E-1	-.79759449E-1	-.37470051E-1
-.72589742E-1	-.32176766E-1	-.58057924E-1	-.23699273E-1	.25473123E+1	.459291
54.90GHz					
.10000000E+1	.56774825E+0	.56048550E+0	.21827777E+0	.60172031E-1	.66808367E-2
-.57212071E-1	-.33412287E-1	-.78157829E-1	-.39469207E-1	-.80146923E-1	-.38211398E-1
-.72951209E-1	-.32815977E-1	-.58350499E-1	-.24171486E-1	.25673943E+1	.460022
58.40GHz					
.10000000E+1	.62976264E+0	.59208608E+0	.24827964E+0	.80379454E-1	.13509334E-1
-.54649687E-1	-.36207737E-1	-.80123911E-1	-.44223746E-1	-.82770825E-1	-.42985301E-1
-.75413257E-1	-.36938696E-1	-.60345256E-1	-.27219927E-1	.26865309E+1	.464224
58.82GHz					
.10000000E+1	.63491862E+0	.59508925E+0	.25163174E+0	.82797327E-1	.14482012E-1
-.54253648E-1	-.36399237E-1	-.80308177E-1	-.44668250E-1	-.83047480E-1	-.43442921E-1
-.75676103E-1	-.37335561E-1	-.60558841E-1	-.27514176E-1	.26998304E+1	.465204
59.40GHz					
.10000000E+1	.64513795E+0	.60078004E+0	.25690628E+0	.86364644E-1	.15797053E-1
-.53734037E-1	-.36816316E-1	-.80640734E-1	-.45466419E-1	-.83516071E-1	-.44254764E-1
-.76119073E-1	-.38038221E-1	-.60918238E-1	-.28034263E-1	.27178708E+1	.465761

CHAPTER 4

MICROWAVE RADIATIVE TRANSFER

4.1 Clear Column Brightness Calculations

For the purpose of calculating the brightness temperature of a given microwave channel at the top of the earth's atmosphere, it is assumed that:

- a) the atmosphere is in local thermodynamic equilibrium,
- b) the atmosphere is plane parallel and horizontally homogenous,
- c) the atmosphere is axially symmetric about nadir-zenith, and
- d) there is no source of illumination exterior to the earth-atmosphere system.

The basic equation of transfer for an absorbing medium can be written:

$$-\frac{dI_v}{k_v \rho ds} = I_v - J_v \quad (4-1)$$

Assuming transfer along a path perpendicular to the surface of the earth, dz can be substituted for ds . The formal solution of Eq. (4-1) is:

$$I_v(z) = I_v(0)e^{-\int_0^z k_v \rho dz'} + \int_0^z J_v(z')e^{-\int_0^z k_v \rho dz'} k_v \rho dz' \quad (4-2)$$

where k_v is the coefficient of gaseous absorption and ρ is the density of absorbing gases. Defining the transmissivity as:

$$\tau_v(z', z) = \exp\left(-\int_{z'}^z k_v \rho dz\right), \quad (4-3)$$

enables equation (4-2) to be written:

$$I_{\nu}(z) = I_{\nu}(0)\tau_{\nu}(0,z) + \int_{z'=0}^z J_{\nu}(z')d\tau_{\nu}(z',z).$$

Therefore, the radiant energy reaching the top of the atmosphere ($z=\infty$) is given by:

$$I_{\nu} = I_{\nu}(0)\tau_{\nu}(0,\infty) + \int_{z'=0}^{\infty} J_{\nu}(z)d\tau_{\nu}(z',\infty) \quad (4-4)$$

Under assumption (a) the radiant energy emitted at any point in the atmosphere is a function of the temperature and frequency and is given by Planck's Function. In the frequency domain the Planck Function is:

$$B_{\nu}(T) = 2h\nu^3/[c^2(e^{h\nu/KT}-1)] \quad (4-5)$$

where ν is frequency, h is Planck's constant, c is the speed of light and K is Boltzman's constant. In the microwave region $h\nu/KT \ll 1$, therefore,

$$\exp(h\nu/KT) = 1+h\nu/KT. \quad (4-6)$$

Then equation (4-5) reduces to

$$B_{\nu}(T) = \left(\frac{2\nu^2 K}{c^2}\right) T = CT. \quad (4-7)$$

In other words for a given frequency the Planck Function is simply a constant times the absolute temperature. Moreover, the equivalent brightness temperature for upwelling intensity I_{ν} may then be defined as

$$I_{\nu} = CT_B(\nu). \quad (4-8)$$

The radiant energy emitted at a given level is isotropic and makes two contributions to the radiant energy reaching the top of the atmosphere:

a) energy emitted in the upward direction travels directly to the top of the atmosphere while suffering a Beer's Law attenuation along its path length due to absorption by atmospheric gases,

b) energy emitted in the downward direction is attenuated by absorption along its path length to the surface, where a portion of it is reflected back upward and then attenuated along its path length to the top of the atmosphere. Mathematically, the contribution (a) reaching the top of the atmosphere from height, z , can be expressed as:

$$T_B^d(\nu, z) = T(z)\tau_\nu(z, \infty). \quad (4-9)$$

The contribution (b) reaching the top of the atmosphere is given by:

$$T_B^r(\nu, z) = T(z)(1 - \epsilon_\nu)\tau_\nu(0, \infty)\tau_\nu(0, z). \quad (4-10)$$

Normally, transmissivities are calculated as:

$$\tau_\nu(z, \infty) = \exp\left(-\int_z^\infty k_\nu \rho dz'\right), \quad (4-11)$$

representing the portion of the upwelling radiance at level z which reaches the top of the atmosphere. It can be easily shown from Eq. (4-3) that:

$$\tau_\nu(0, z) = \tau_\nu(0, \infty)/\tau_\nu(z, \infty) \quad (4-12)$$

Similarly,

$$\tau_\nu(z', z) = \tau_\nu(z', \infty)/\tau_\nu(z, \infty) \quad (4-13)$$

for any layer defined by z' and $z(z' < z)$.

To obtain the total atmospheric contribution to radiance reaching the top of the atmosphere in any channel, simply integrate equations (4-9) and (4-10) and add them together:

$$\begin{aligned} T_B^a(\nu) = T_B^d(\nu) + T_B^r(\nu) = & \int_{z=0}^{\infty} T(z) d\tau_\nu(z, \infty) \\ & + (1 - \epsilon_\nu) \tau_\nu(0, \infty) \int_{z=0}^{\infty} T(z) d\tau_\nu(0, z) \end{aligned} \quad (4-14)$$

This can be approximated numerically as:

$$T_B^a(\nu) = \sum_i \bar{T}_i \Delta_i \tau_\nu(z, \infty) + (1 - \epsilon_\nu) \tau_\nu(0, \infty) \sum_i \bar{T}_i \Delta_i \tau_\nu(0, z) \quad (4-15)$$

The surface of the earth emits in the microwave range as a grey body. Therefore, the background emission of the earth's surface attenuated to the top of the atmosphere by Beer's Law is given by:

$$T_B^e(\nu) = \epsilon_\nu T_s \tau_\nu(0, \infty) \quad (4-16)$$

Combining equations (4-15) and (4-16).

$$T_B(\nu) = [\epsilon_\nu T_s + \sum_i \bar{T}_i (1 - \epsilon_\nu) \Delta_i \tau_\nu(0, z)] \tau_\nu(0, \infty) + \sum_i \bar{T}_i \Delta_i \tau_\nu(z, \infty). \quad (4-17)$$

Now note that:

$$\begin{aligned} \Delta_i \tau_\nu(0, z) &= \tau_\nu(0, z_i) - \tau_\nu(0, z_{i+1}) \\ &= \frac{\tau_\nu(0, \infty)}{\tau_\nu(z_i, \infty)} - \frac{\tau_\nu(0, \infty)}{\tau_\nu(z_{i+1}, \infty)} \\ &= \frac{\tau_\nu(0, \infty) [\tau_\nu(z_{i+1}, \infty) - \tau_\nu(z_i, \infty)]}{\tau_\nu(z_i, \infty) \tau_\nu(z_{i+1}, \infty)} \end{aligned}$$

$$= \left[\frac{\tau_v(0, \infty)}{\tau_v(z_i, \infty) \tau_v(z_{i+1}, \infty)} \right] \Delta_i \tau_v(z, \infty)$$

Therefore equation (4-17) can be written:

$$T_B(v) = \epsilon_v T_s \tau_v(0, \infty) + \sum_{i=1}^{n-1} [(1-\epsilon_v) \frac{\tau_v(0, \infty)^2}{\tau_v(z_i, \infty) \tau_v(z_{i+1}, \infty)} + 1] \bar{T}_i \Delta_i \tau_v(z, \infty) \quad (4-18)$$

where n is the number of levels used to represent the atmosphere. This is simply the approximation to:

$$T_B(v) = \epsilon_v T_s \tau_v(0, \infty) + \int_{z=0}^{\infty} [(1-\epsilon_v) \tau_v(0, z)^2 + 1] T(z) d\tau_v(z, \infty) \quad (4-19)$$

Equation (4-19) is the absorption/emission solution, equation (4-4), to the radiative transfer equation where,

$$I_v(0) = C \epsilon_v T_s \quad (4-20)$$

and

$$J_v(z) = C T(z) [(1-\epsilon_v) \tau_v(0, z)^2 + 1] \quad (4-21)$$

This is a good approximation for a clear atmosphere where scattering in the microwave region is very small. Note that equation (4-19) yields what is commonly referred to as antenna temperature if the transmissivities used have been corrected to include antenna gain characteristics. With unaltered transmissivities equation (4-19) yields the clear column brightness temperature.

4.2 Brightness Calculations for Cloudy Atmospheres

The basic equation of transfer for a plane parallel cloud layer in local thermodynamic equilibrium can be written in the form:

$$\mu dI_{\nu}(\tau, \mu)/d\tau = I_{\nu}(\tau, \mu) - \bar{\omega}_{\nu}/2 \int_{-1}^1 P_{\nu}(\mu, \mu') I_{\nu}(\tau, \mu') d\mu' - (1 - \bar{\omega}_{\nu}) B_{\nu}[T(\tau)] \quad (4-22)$$

where I_{ν} represents the monochromatic radiance, μ the cosine of the emergent angle with respect to the zenith, τ the monochromatic optical depth, P_{ν} the normalized axially symmetrical scattering phase function and $\bar{\omega}_{\nu}$ the single scattering albedo. $B_{\nu}[T(\tau)]$ is the Planck Function as defined by equation (4-7). The normalized phase function can be expressed as a Legendre polynomial of finite terms. By approximating the integration in equation (4-22) utilizing Gauss' quadrature formula, a set of first order inhomogeneous differential equations can be derived. The homogeneous and particular solutions of the differential equations as outlined by Chandrasekhar (1950), enables the complete solution of the scattered intensity from an isothermal cloud (temperature, T_c) for a given discrete stream to be expressed as:

$$I_{\nu}(\tau, \mu_i) = \sum_m L_m \phi_m(\mu_i) \exp(-k_m \tau) + B_{\nu}(T_c) \quad (4-23)$$

where m is the number of discrete streams employed, ϕ_m and k_m represent eigen functions and eigen values for the differential equations and L_m are a set of constants of proportionality which can be determined from the radiation boundary conditions. Noting that the brightness temperature in the microwave range is simply the radiant intensity derived by a constant, equation (4-22) can also be written in terms of brightness

temperature. The associated solution is then given by:

$$T_B(\nu, \tau; \mu_i) = \sum_m L_m \theta_m(\mu_i) \exp(-k_m \tau) + T_c \quad (4-24)$$

where the constants of proportionality, L_m , are different from those in equation (4-23), having been obtained using brightness boundary conditions. T_c is the cloud layer temperature and is independent of frequency, ν .

At the cloud top, the downward brightness is equal to the brightness contributions from every point in the atmosphere above the cloud top attenuated by Beer's Law to the cloud top. This can be expressed as:

$$T_B(\nu, z_t; -\mu_i) = \int_{z=z_t}^{\infty} T(z) d\tau_\nu(z, z_t; -\mu_i) \quad (4-25)$$

where z_t is the height at the cloud top and the negative sign on μ_i simply indicates downward transfer. Note that:

$$\tau_\nu(z_t, z; \mu_i) = \tau_\nu(z, z_t; -\mu_i) = \exp[-(\tau_t - \tau)/\mu_i] \quad (4-26)$$

and

$$\tau_\nu(z_1, z_2; \mu_i) = \tau_\nu(z_1, \infty; \mu_i) / \tau_\nu(z_2, \infty; \mu_i) \quad (4-27)$$

where $z_2 > z_1$

Within the cloud layer, where scattering occurs, continuity of brightness values from all directions is required. Thus:

$$T_B(\nu, z_\ell; \mu_i) = T_B(\nu, z_{\ell+1}; \mu_i) \quad \ell=1, 2, \dots, N-1 \quad (4-28)$$

where N is the total number of sublayers within the cloud.

At the lower boundary of the cloud, three brightness contributions are immediately apparent:

- a) the surface contribution,
- b) the direct atmospheric contribution from below the cloud and
- c) the reflected atmospheric contribution from below the cloud.

A fourth, and perhaps less obvious, brightness contribution at the lower boundary must be considered. Since the reflection of downward brightness by the earth's surface is significant for microwave radiation, the emergent brightness at the cloud bottom will contribute to the lower boundary condition. That is to say, the solution to the radiative transfer through the cloud effects the boundary conditions used to obtain the solution. This suggests that an iterative approach to the correct solution is required. Practically, this is accomplished by assuming initially that the top/down throughput of the cloud equals one. The emergent intensity at the cloud bottom obtained by this assumption can then be attenuated by two trips through the atmosphere between the earth's surface and the cloud base and by the reflection at the earth's surface. This value is added to the lower boundary condition and the solution to the radiative transfer equation then produces a new value for the emergent brightness at the cloud bottom. From this solution a new top/down throughput can be calculated and the process is repeated until the new throughput varies from the old by less than one tenth. In all cases examined by this study the iteration halted after only two steps. The lower boundary condition can then be expressed as:

$$\begin{aligned}
T_B(\nu, z_b; \mu_i) = & \epsilon_\nu T_s \tau_\nu(0, z_b; \mu_i) + \int_{z=0}^{z_b} T(z) d\tau_\nu(z, z_b; \mu_i) \\
& + (1 - \epsilon_\nu) \tau_\nu(0, z_b; \mu_i) \left[\int_{z=0}^{z_b} T(z) d\tau_\nu(0, z; -\mu_i) \right. \\
& \left. + T_B(\nu, z_t; -\mu_i) T_p(\mu_i) \tau_\nu(0, z_b; \mu_i) \right]
\end{aligned} \tag{4-29}$$

where $T_p(\mu_i)$ is defined to be the top/down throughput of the cloud for the stream defined by μ_i and z_b is the height of the cloud base.

$$T_p(\mu_i) = T_B(\nu, z_b; -\mu_i) / T_B(\nu, z_t; -\mu_i) \tag{4-30}$$

The solution of the microwave transfer equation given by equation (4-24) is applicable only to isothermal and homogeneous cloud layers. To apply the transfer solution to thick clouds it is necessary to divide the cloud into sublayers for which the isothermal and homogeneous assumptions are reasonable. By matching the brightness continuity equation for brightness in each sublayer, a set of linear equations with unknown coefficients can be obtained which can be solved by standard matrix inversion techniques. Similar procedures have been used by Liou (1975) to evaluate the transfer of solar radiation in inhomogeneous atmospheres and by Feddes and Liou (1977) to investigate the transfer of spectral infrared radiation in cloudy atmospheres.

CHAPTER 5

SENSITIVITY TO CLOUD LAYERS

Sections 5.1 through 5.4 of this chapter are descriptive in nature. The profiles and cloud models used are discussed in section 5.1. Sections 5.2 through 5.5 simply report the results obtained with no attempt at explanation. Section 5.5 deals with the interpretation of the results and the physical mechanisms which produced them.

5.1 Profiles and Cloud Models Used

Two climatological profiles were used for this sensitivity study. The first profile was derived from the Northern Hemispheric Mid-Latitude Spring/Fall climatology contained in the U.S. Standard Atmospheric Supplements, 1966. The second profile was derived from the climatology for 30° North Latitude, July, contained in the same source. For both profiles temperature and height values were interpolated to 40 standard pressure levels used for this study. Mixing ratio values for levels below 250 mb were obtained from a Skew-T Diagram and hence are saturation values. Above 250 mb a constant mixing ratio of 3 parts per million was used. The resulting Mid-Latitude Spring/Fall profile is given in Table 17, while the 30° N. Latitude, July, profile is contained in Table 18.

Cloud models of 1, 2, 3, 4 and 5 Km thicknesses were investigated, employing the Marshall-Palmer drop size distribution to simulate rainfall rates of 1, 2, 3, 4, 5, 10, 15, 20, 25 and 30 mm/hr. In addition,

Table 17. N. Hemisphere Mid-Latitude Spring/Fall Profile

Pres(mb)	Height(Km)	Temp(°K)	H ₂ O Vapor(gm/m ³)
1000.00	.110	287.42	.1240E+2
950.00	.540	284.64	.1049E+2
920.00	.810	282.90	.9248E+1
899.54	1.000	281.70	.8625E+1
850.00	1.460	278.67	.7138E+1
794.81	2.000	275.12	.5682E+1
780.00	2.150	274.13	.5298E+1
700.89	3.000	268.64	.3530E+1
700.00	3.010	268.57	.3511E+1
670.00	3.360	266.32	.3094E+1
620.00	3.960	262.43	.2254E+1
616.78	4.000	262.17	.2213E+1
570.00	4.600	258.24	.1625E+1
540.60	5.000	255.66	.1349E+1
500.00	5.580	251.85	.9800E+0
475.00	5.960	249.47	.8078E+0
472.41	6.000	249.21	.7920E+0
430.00	6.680	244.77	.5391E+0
400.00	7.190	241.44	.3875E+0
356.57	8.000	236.19	.2374E+0
350.00	8.130	235.34	.2154E+0
300.00	9.180	228.54	.1061E+0
265.03	10.000	223.23	.6446E-1
250.00	10.380	220.73	.4735E-1
200.00	11.810	216.65	.9650E-3
194.29	12.000	216.65	.9374E-3
150.00	13.650	216.65	.7237E-3
135.00	14.310	216.65	.6513E-3
115.00	15.330	216.65	.5549E-3
100.00	16.220	216.65	.4825E-3
85.00	17.260	216.65	.4101E-3
70.00	18.500	216.65	.3377E-3
60.00	19.480	216.65	.2895E-3
50.00	20.640	217.26	.2406E-3
30.00	23.940	220.51	.1422E-3
25.00	25.130	221.69	.1179E-3
20.00	26.590	223.14	.9369E-4
15.00	28.500	225.02	.6968E-4
10.00	31.210	227.18	.4601E-4
7.00	33.630	224.11	.3265E-4
5.00	35.980	239.14	.2186E-4
4.00	37.580	243.94	.1714E-4
3.00	39.680	249.62	.1256E-4
2.00	42.730	258.02	.8102E-5
1.50	44.950	264.05	.5938E-5
1.00	48.180	270.52	.3864E-5
.50	53.760	267.65	.1953E-5
.20	60.880	253.96	.8232E-6
.10	65.960	235.47	.4439E-6

Table 18. 30° N. Latitude July Profile

Pres(mb)	Height(Km)	Temp(°K)	H ₂ O Vapor(gm/m ³)
1000.00	.120	303.51	.3107E+2
950.00	.570	299.44	.2411E+2
920.00	.850	297.12	.2182E+2
904.78	1.000	296.12	.2071E+2
850.00	1.540	292.36	.1676E+2
805.30	2.00	289.61	.1424E+2
780.00	2.270	287.99	.1283E+2
714.56	3.000	283.73	.9815E+1
700.00	3.170	282.73	.9158E+1
670.00	3.540	280.60	.8115E+1
633.18	4.000	277.92	.6794E+1
620.00	4.170	276.92	.6329E+1
570.00	4.850	273.05	.4914E+1
559.45	5.000	272.21	.4655E+1
500.00	5.890	267.16	.3235E+1
493.03	6.000	266.43	.3049E+1
475.00	6.290	264.51	.2573E+1
430.00	7.050	259.10	.1738E+1
400.00	7.600	255.25	.1257E+1
379.05	8.000	252.45	.1024E+1
350.00	8.590	248.31	.7105E+0
300.00	9.700	240.53	.3607E+0
287.37	10.000	238.44	.3062E+0
250.00	10.960	231.66	.1514E+0
214.13	12.000	224.48	.7763E-1
200.00	12.450	221.31	.5005E-1
150.00	14.260	208.69	.5159E-2
135.00	14.910	204.20	.6911E-3
115.00	15.870	203.20	.5916E-3
100.00	16.710	204.56	.5110E-3
85.00	17.690	206.71	.4298E-3
70.00	18.889	209.31	.3496E-3
60.00	19.840	211.40	.2967E-3
50.00	20.980	213.89	.2444E-3
30.00	24.260	220.41	.1423E-3
25.00	25.450	222.78	.1173E-3
20.00	26.930	225.71	.9262E-4
15.00	28.860	229.54	.6831E-4
10.00	31.650	235.10	.4446E-4
7.00	34.160	240.79	.3039E-4
5.00	36.600	246.56	.2120E-4
4.00	38.240	250.45	.1669E-4
3.00	40.400	255.58	.1227E-4
2.00	43.530	262.96	.7950E-5
1.50	45.790	268.31	.5844E-5
1.00	49.070	272.08	.3842E-5
.50	54.650	265.65	.1967E-5
.20	61.700	248.11	.8426E-6
.10	66.670	230.02	.4544E-6

the significance of cloud position was investigated by varying the base of a 2 Km thick cloud employing the drop size distribution of the Deirmendjian L-Model cloud.

For spherical particles the droplet volume per unit volume of atmosphere is given by:

$$V = \frac{4}{3} \pi \int_0^{\infty} r^3 N(r) dr . \quad (5-1)$$

Therefore the total liquid water content per unit volume of atmosphere is:

$$\bar{W} = \frac{4}{3} \pi \rho \int_0^{\infty} r^3 N(r) dr \quad \text{gm cm}^{-3} \quad (5-2)$$

where r is in units of cm, $N(r)$ is in terms of cm^{-4} and the density of liquid water is 1 gm cm^{-3} . For the Deirmendjian L-Model

$$\bar{W} = 1.16678(10^{-2}) \quad \text{gm cm}^{-2} \text{ Km}^{-1} \quad (5-3)$$

while for the Marshall-Palmer size distribution

$$\bar{W} = 8.89415(10^{-3}) R^{.84} \quad \text{gm cm}^{-2} \text{ Km}^{-1} . \quad (5-4)$$

Table 19 contains the total mass of liquid water within a column of 1 cm^2 cross section for the cloud models used.

5.2 Dependence on Layer Thickness and Rainfall Rate

To determine the effect of varying cloud thicknesses on the brightness temperatures reaching the top of the atmosphere, cloud models were inserted into the atmosphere with a constant cloud base of 1 Km. Thickness cases of 1, 2, 3, 4 and 5 Km were examined. Variation of brightness temperatures over land with respect to cloud thickness and rainfall

Table 19. Total Liquid Water Content (10^{-2} gm cm $^{-2}$)

Thickness (Km)	1	2	3	4	5
Deirmendjian:	1.16678	2.33356	3.50034	4.66712	5.83390
Marshall-Palmer:					
R(mm/hr)					
1	0.88941	1.77882	2.66823	3.55764	4.44705
2	1.59209	3.18418	4.77627	6.36835	7.96044
3	2.23812	4.47625	6.71437	8.95249	11.1906
4	2.84992	5.69984	8.54975	11.3997	14.2496
5	3.43745	6.87491	10.3124	13.7498	17.1873
10	6.15321	12.3064	18.4596	24.6129	30.7661
15	8.65005	17.3001	25.9502	34.0020	43.2503
20	11.0146	22.0291	33.0437	44.0583	55.0728
25	13.2853	26.5706	39.8559	53.1412	66.4266
30	15.4840	30.9681	46.5421	61.9361	77.4201

rate for channels 1 through 4 are displayed in Figures 3 through 7. Figures 8 through 11 depict the variation of brightness temperatures over ocean with respect to cloud thickness and liquid water content for the same channels. The energy sensed by channels 5, 6 and 7 originates sufficiently high in the atmosphere that the brightness temperatures are insignificantly effected by the cloud models.

The differences due to thickness for channels 3 and 4 may be misleading. It is more likely that a positional dependence for the cloud is being exhibited. Since the cloud base was fixed at 1 Km, only the thicker clouds reached into the energy source regions for channels 3 and 4 (weighting functions peak at about 7 and 10.5 Km, respectively). For example, a 5 Km thick cloud with a 1 Km base at a 2 mm/hr rainfall rate results in brightness temperatures for channels 3 and 4 of 237.3 °K and 228.9 °K. The Deirmendjian L- Model cloud used in the position study has liquid water content approximately equal to that of the 2 mm/hr rain model (see Table 19) and yet a 2 Km

thick L-Model cloud with base at 4 Km results in nearly the same brightness temperatures for channels 3 and 4 as the 5 Km thick cloud discussed above (237.2°K and 228.7°K, respectively).

5.2.1 Over Land

Channels 1 and 2 (peaking near the surface and 2 Km) show decreasing brightness temperatures for increasing cloud thicknesses. The decrease is greater for clouds modeling higher rainfall rates. For channel 1 at a rainfall rate of 1 mm/hr the decrease ranges from 2°K for a 1 Km thick cloud to 16°K for a 5 Km thick cloud. For a rainfall rate of 30 mm/hr the channel 1 brightness temperature decreases 14°K for a 1 Km thick cloud and 43°K for a 5 Km thick cloud. Channel 2 displays the same trends as channel 1 but to a lesser degree. For a rainfall rate of 1 mm/hr the decrease in channel 2 brightness as a function of cloud thickness ranges from less than .5°K to 5°K. For a rainfall rate of 30 mm/hr the range is 4°K to 22°K.

Channels 3 and 4 result in relatively constant (unaffected) brightness temperatures for light rainfall rates (less than 3mm/hr). For rainfall rates greater than 3 mm/hr the brightness temperature decreases with increasing cloud thickness. The maximum decreases are 7°K for channel 3 and 2°K for channel 4; both at rainfall rates of 30 mm/hr and cloud thicknesses of 5 Km.

5.2.2 Over Ocean

The results over the ocean are quite different from the results over land. The only physical difference between these two cases is that the surface emissivity for all channels is taken to be .97 for a land surface and .51 for an ocean surface. This effects two of the transfer terms:

1) the surface contribution over ocean is approximately one half of the surface contribution over land ($\epsilon=.97$, $\epsilon=.51$), and

2) the atmospheric contribution reflected from the earth's surface is approximately 16 times greater over the ocean ($r=.03$, $r=.49$).

Figures 8 and 9 show that channels 1 and 2 follow similar trends over the ocean but to different degrees. For all cloud thicknesses an initial reduction in brightness temperature is observed for clouds with low liquid water content. For channel 1 the maximum reduction is 2°K while for channel 2 the maximum reduction is nearly 13°K . At some liquid water content less than $5(10^{-2})\text{ gm cm}^{-2}$ the brightness begins to increase. The turning point occurs at lower liquid water content for thinner clouds. The brightness then increases until the liquid water content nears $15(10^{-2})\text{ gm cm}^{-2}$. For channel 1 this increase results in a maximum brightness over 35°K higher than the clear column value. For channel 2 the maximum brightness is about 3°K greater than the clear column value. For liquid water contents greater than $15(10^{-2})\text{ gm cm}^{-2}$ brightness decreases for both channels and all cloud thicknesses. Note, the maximum brightness observed over the ocean is very nearly the same as the minimum brightness observed over the land.

Figures 10 and 11 indicate that channels 3 and 4 are relatively unaffected by a 1 Km thick cloud with a cloud base at 1 Km. Increasing the cloud thickness above 1 Km causes steadily decreasing brightness temperatures. For a constant cloud thickness, increasing the liquid water content causes a decrease in brightness. Note that channel 4 is effected by less than 1°K for all of the cases studied.

5.3 Dependence on Layer Location

Figures 12 through 23 display the importance of cloud position relative to the peak of the weighting function for each channel.

Channels 1 and 2 show the effects on a channel when the cloud is at or above the peak of the weighting function, i.e., the prime energy source region for the channel. The brightness temperature decreases rapidly as the cloud is moved higher putting more and more of the energy source for the channel beneath it. Eventually, the brightness becomes near constant as all of the significant source region for channel energy is below the cloud and therefore raising the cloud higher has only slight effects.

Channels 3 and 4 show the results of moving a cloud from below the energy source region up through the source region. Far below the energy source the brightness temperature remains nearly constant. Then, as the cloud moves into the source region, the brightness temperature decreases significantly, becoming near constant above the source region as for channels 1 and 2.

Channels 6 and 7 indicate that for channels peaking high enough in the atmosphere to be free of surface effects, brightness temperatures increase slightly as the cloud approaches the energy source region from below.

Figures 18 through 23 indicate that the same positional dependence exists over the ocean as over the land with no change in trends for any of the channels.

5.4 Dependence on Profile

Figures 24 through 31 display the results when the sensitivity analysis is duplicated for the 30°N. Latitude, July, profile. Although

the different profile naturally results in different brightness temperatures, the trends noted for the N. Hemispheric Mid-Latitude Spring/Fall profile are observed to persist.

5.5 Interpretation of Results

In order to aid in the interpretation of results Figure 32 is included which graphically depicts the terms contributing to the cloud boundary conditions and the mechanisms for energy loss and gain within the cloud. There are three mechanisms for energy gain within the cloud (gaseous emission, droplet emission and multiple scattering) and there are three mechanisms for energy loss (gaseous absorption, droplet absorption and single scattering). The balance of these mechanisms determine whether the emergent energy at the cloud top and bottom is greater or less than the respective boundary condition at the cloud bottom and top. Of course, the boundary conditions themselves are an important contribution to the emergent energy at the opposite side of the cloud. The upper boundary condition is totally unaffected by the earth's surface. For the lower boundary condition, quite the opposite is true. When the emissivity (and hence the reflectivity) of the earth's surface varies, three of the four contributing terms for the lower boundary condition are effected:

- 1) the surface emission term,
- 2) the atmospheric contribution reflected from the surface of the earth, and
- 3) the emergent energy from the cloud bottom reflected from the earth's surface. Finally, it is important to note that the emission terms are generally stronger near the cloud bottom due to the temperature gradient within the cloud; and throughout the cloud, emission by

water droplets is greater than emission by atmospheric molecules.

Introducing a cloud into the atmosphere will then result in increased emission within the cloud layer and decreased transmissivity through the cloud layer. The three contributions to cloud top brightness are emission by the earth's surface, atmospheric emission and emission from within the cloud layer.

To turn off the surface term, atmospheric contribution or cloud emission simply set the surface temperature, boundary conditions or cloud temperature equal to zero, respectively. Each contribution can be analyzed separately by turning off the other two.

Figures 33 through 36 display the effects over the ocean of cloud thickness and liquid water content on the three contributions to cloud top brightness. The solid line is the graphical sum of these components and the X's are computed cloud top temperatures for randomly selected cases. Clearly, the addition to channel 1 energy by droplet emission is greater than the energy loss due to droplet absorption and single scattering for liquid water contents greater than $.01 \text{ gm cm}^{-2}$. This explains the region of increasing brightness temperature for channel 1 observed in Figure 8. For liquid water content greater than $.20 \text{ gm cm}^{-2}$ the droplet emission reaching the cloud top is nearly constant and represents almost all of the energy reaching the cloud top. Although the surface emission and atmospheric contributions to cloud top brightness are small in this region, they are decreasing with increasing liquid water content so the cloud top brightness decreases slightly also. This explains the slight decrease in channel 1 brightness temperature in this region. The fact that cloud emission accounts

for almost all of the cloud top brightness for water content greater than $.20 \text{ gm cm}^{-2}$ explains why the brightness temperatures over the ocean and over the land are nearly the same in this region. The cloud emission must be less than the reduction in the surface and atmospheric terms for liquid water content less than $.01 \text{ gm cm}^{-2}$ in order to explain the slight decrease in brightness temperatures in this region.

Over the land the cloud emission curves remain the same. As previously noted, the surface term is nearly twice as large over land while the reflected terms are only one sixteenth as large. The direct atmospheric contribution remains the same. The net result is that over land the upwelling brightness at the cloud bottom is significantly larger than over the ocean. For example, the lower boundary condition over land for a 1 Km thick cloud ranges from 280°K to 285°K for rainfall rates of 1 to 30 mm/hr. Over the ocean the range is 200°K to 240°K for the same cloud thickness and rainfall rates. Since the loss of energy within the cloud layer is proportional to the energy incident at the cloud base, a greater reduction takes place over the land. This increased reduction is larger than the increase by cloud emission which explains why brightness temperatures for channel 1 continuously decrease with increasing liquid water content over land (see Figures 3 through 7).

For channel 2 (see figures 35 and 36) the surface contribution to cloud top brightness over the ocean is less than that for channel 1 due to the differences in transmissivity. The atmospheric terms are increased, however, due to the shape of the weighting function for this channel and the high reflectivity of the ocean surface. The net result is a higher cloud top brightness for channel 2. The lower boundary

condition is also higher for the same reasons, resulting in a greater reduction in the surface and atmospheric terms as they traverse the cloud. This explains the deepening of the reduction in brightness for liquid water contents less than $.05 \text{ gm cm}^{-2}$ (see Figure 9). It also explains why the increase in brightness for liquid water contents of $.05$ through $.15 \text{ gm cm}^{-2}$ is not as large as the corresponding increases for channel 1. Note that energy emitted by the cloud is approximately the same for both channels.

Nearly the same discussion applies for channel 2 over land as for channel 1. The surface term increases due to the change in emissivity of the earth's surface. The increase is smaller than for channel 1, however, due to transmissivity differences. The atmospheric terms decrease due to the change in reflectivity of the earth's surface. The decrease is larger than for channel 1 due to the shape of the weighting functions. The net result is that the lower boundary condition increases for channel 2 over land, but the increase is much less than for channel 1. For example, for a 1 Km thick cloud and rainfall rates of 1 and 30 mm/hr the lower boundary condition for channel 2 is nearly constant at 285°K over land but ranges from 250°K to 265°K over the ocean. Once again, this increase in the lower boundary condition results in increased reduction through the cloud resulting in continuously decreasing brightness temperatures with increasing rainfall rates.

Channels 3 and 4 are relatively unaffected by the emissivity of the earth's surface. This is due to the fact that the transmissivity from the earth's surface to the top of the atmosphere is only .023 for channel 3 and .003 for channel 4. This explains why the brightness temperatures for channels 3 and 4 do not vary much between land and

ocean surfaces. The highest cloud top modeled was at 6 Km. This is just below the peak of the weighting function for channel 3 (7 Km) but still well below the peak for channel 4 (10.5Km). As the cloud top moves into the energy source regions for these channels emission by the cloud is lower since the temperatures are lower at higher altitudes. Furthermore, the transmissivity from 6 Km to the top of the atmosphere is less than .3 for both channels. Therefore, within the energy source region occupied by the upper portion of the cloud, the extinction mechanisms dominate over the mechanisms for adding energy, resulting in slight decreases in brightness temperatures.

The interpretation of cloud position dependence illustrated by Figures 12 through 23 is quite straight forward. Note that the lowest cloud base examined is at 1 Km where the brightness temperatures over ocean for channels 1 and 2 are 265.5°K and 255.2°K, respectively. These values are higher than clear column values due to the fact that cloud emission exceeds extinction for a 2 Km thick cloud with a base at 1 Km for liquid water contents greater than $.01 \text{ gm cm}^{-2}$ (see Figures 33 through 36). The liquid water content for the 2 Km thick L-Model cloud is $.23 \text{ gm cm}^{-2}$ (see Table 19). As the cloud is moved higher in the atmosphere two changes take place. The emission by the cloud reduces due to the reduction in cloud temperature and the lower boundary condition increases because a greater portion of the energy source regions for channels 1 and 2 is below the cloud base. This results in increased energy reduction within the cloud layer. The net result is that brightness temperatures for channels 1 and 2 decrease as the cloud is moved higher up in the atmosphere. Eventually, the cloud is raised high enough that nearly all of the energy source regions for channels

1 and 2 are already below the cloud and cloud temperatures are sufficiently low that emission by the cloud is very small. Then moving the cloud still higher has very little effect and brightness temperatures are nearly constant. The same discussion applies over land except that over land even the 1 Km cloud base results in a reduction in brightness temperatures from the clear column values.

Channels 3, 4, 6 and 7 have weighting functions which peak higher in the atmosphere, reducing the effects of surface emissivity. Therefore, the effects of a 2 Km thick cloud are basically the same over ocean and land surfaces. For clouds well below the peak of the weighting functions the cloud has no effect on channel brightness. This is because there is no significant energy source below the cloud to be reduced by the cloud extinction and the transmissivity from the cloud top to the top of the atmosphere is sufficiently small that emission by the cloud is negligible. As the cloud moves into the energy source region a delicate trade off of cloud emission and extinction takes place. For channels 3 and 4 this trade off holds the brightness temperatures very nearly constant until the cloud is well into the energy source region. For channels 6 and 7 a very slight increase in brightness temperatures is noted. This increase is less than $.2^{\circ}\text{K}$, however, which is below the noise level of the SSM/T. Finally, as the cloud is moved above the peaks of the weighting functions brightness temperatures decrease, eventually becoming near constant as for channels 1 and 2.

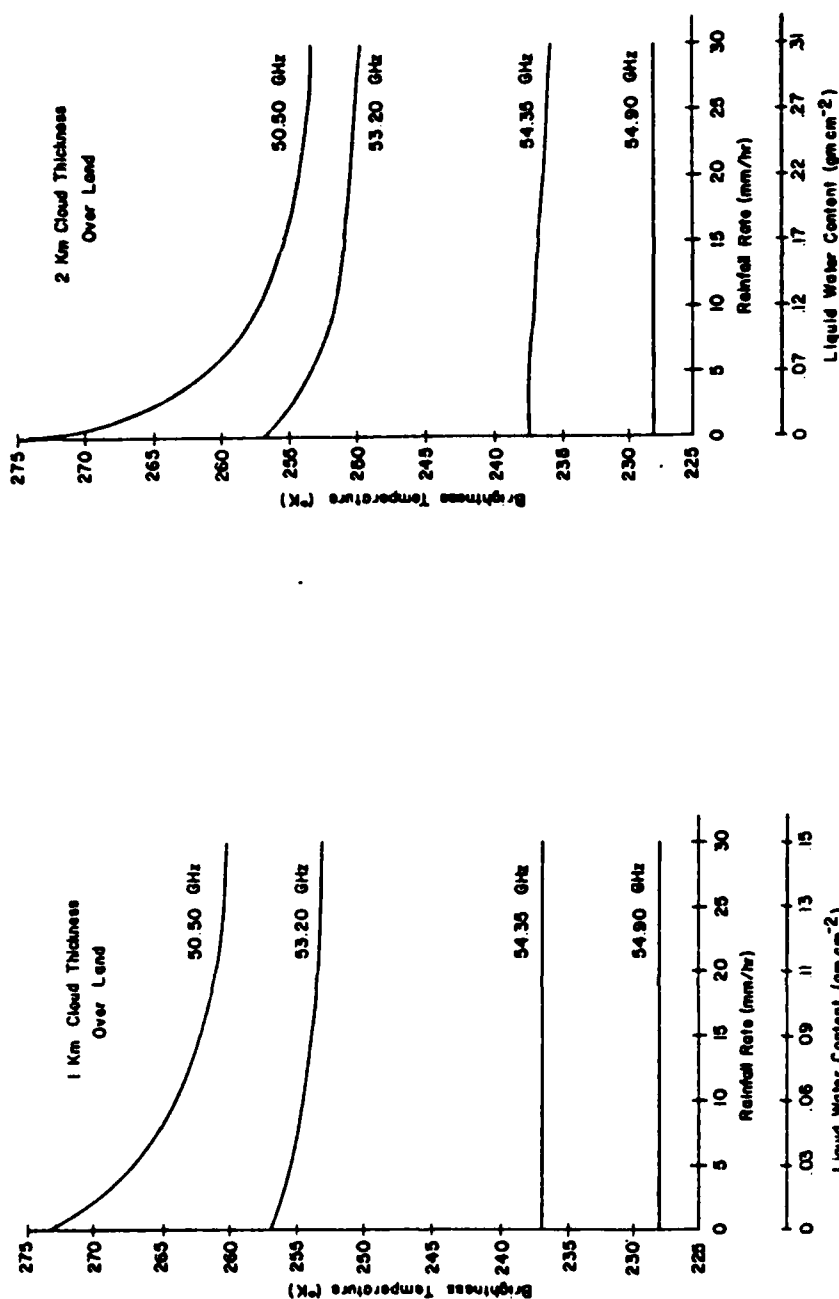


Figure 3. Brightness temperature vs rainfall rate (or liquid water content) for 1 Km thick cloud over land (Mid-Latitude Spring/Fall profile).

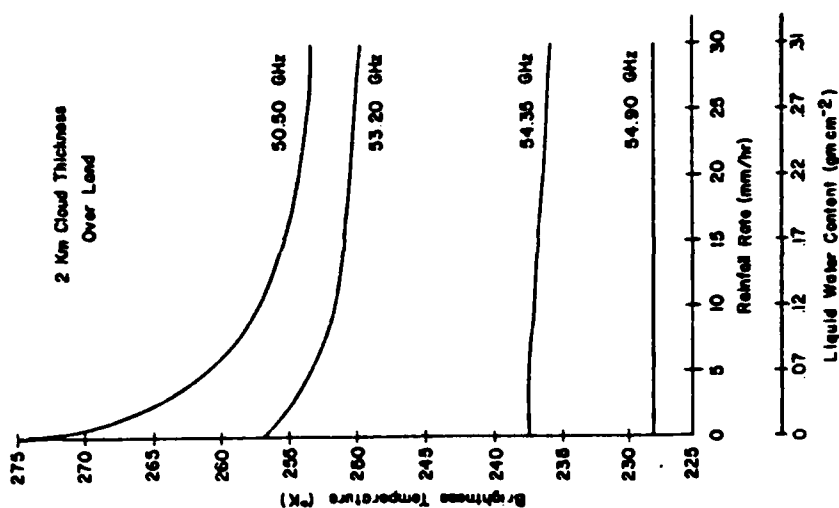


Figure 4. Brightness temperature vs rainfall rate (or liquid water content) for 2 Km thick cloud over land (Mid-Latitude Spring/Fall profile).

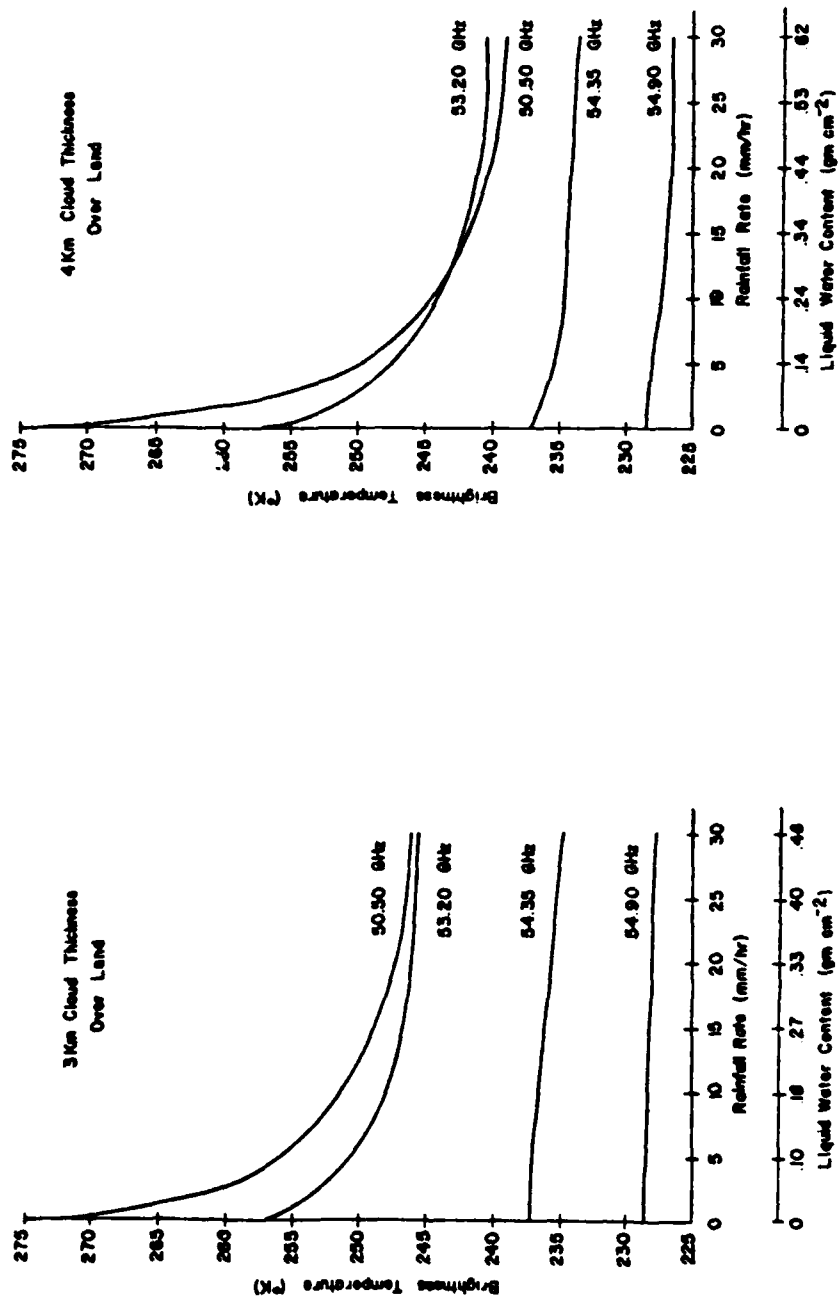


Figure 5. Brightness temperature vs rainfall rate (or liquid water content) for 3 Km thick cloud over land (Mid-Latitude Spring/Fall profile).

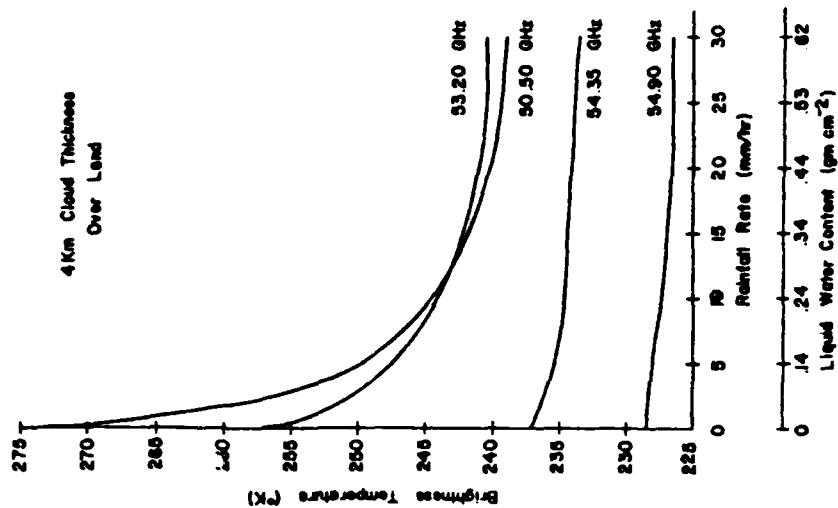


Figure 6. Brightness temperature vs rainfall rate (or liquid water content) for 4 Km thick cloud over land (Mid-Latitude Spring/Fall profile).

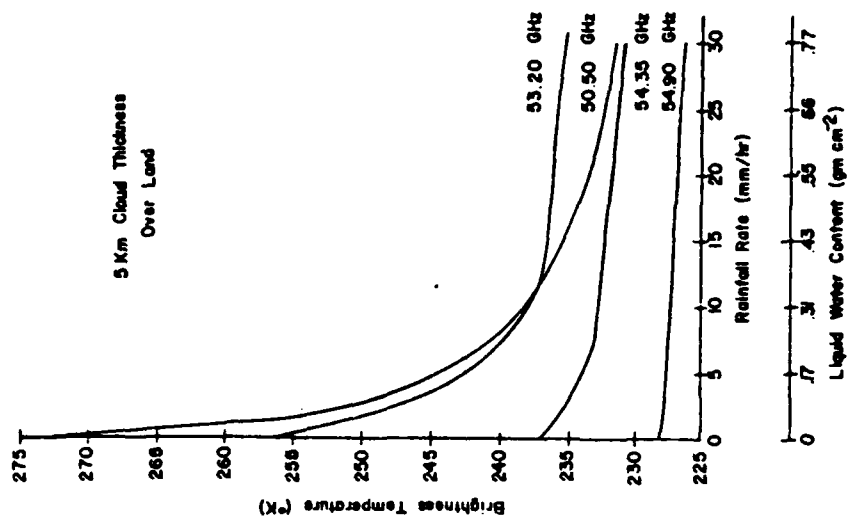


Figure 7. Brightness temperature vs rainfall rate (or liquid water content) for 5 Km thick cloud over land (Mid-Latitude Spring/Fall profile).

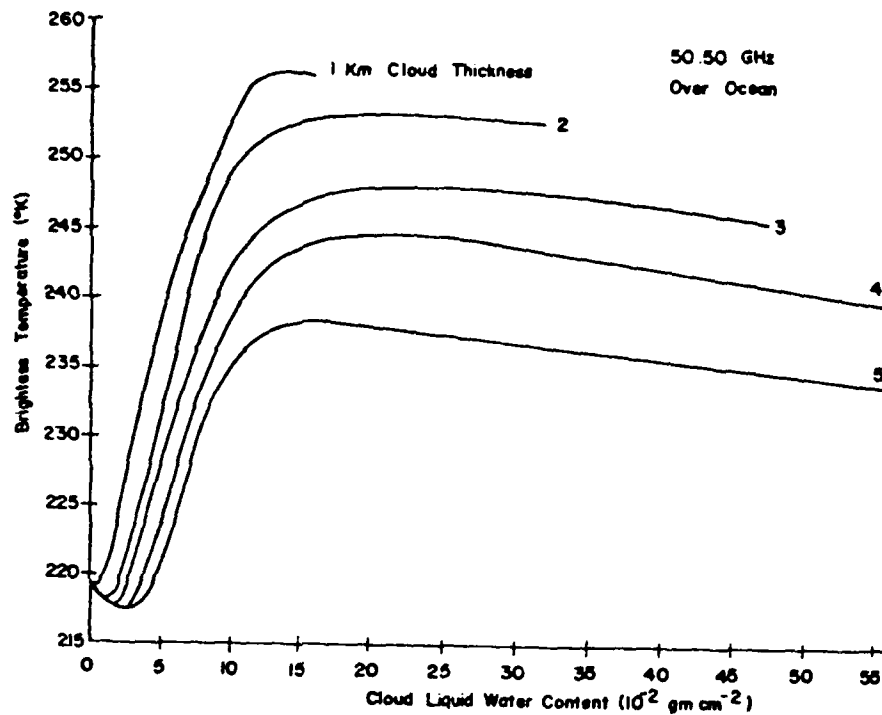


Figure 8. 50.50 GHz brightness temperature as a function of cloud thickness and liquid water content (Mid-Latitude Spring/Fall profile over ocean).

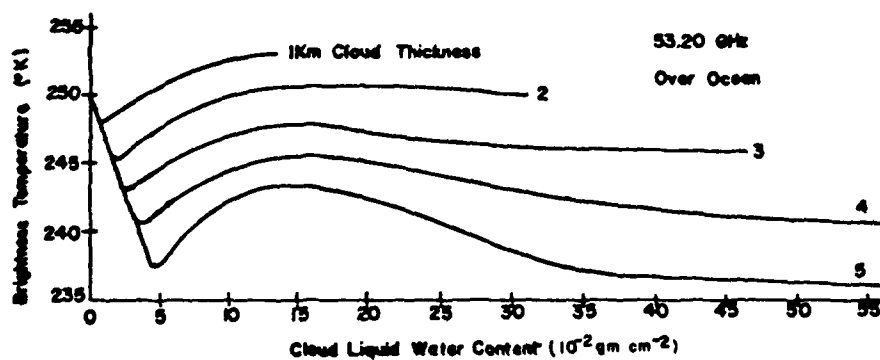


Figure 9. 53.20 GHz brightness temperature as a function of cloud thickness and liquid water content (Mid-Latitude Spring/Fall profile over ocean).

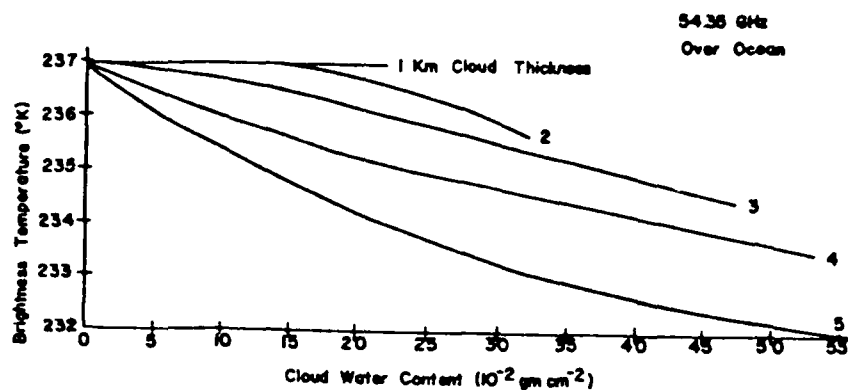


Figure 10. 54.35 GHz brightness temperature as a function of cloud thickness and liquid water content (Mid-Latitude Spring/Fall profile over ocean).

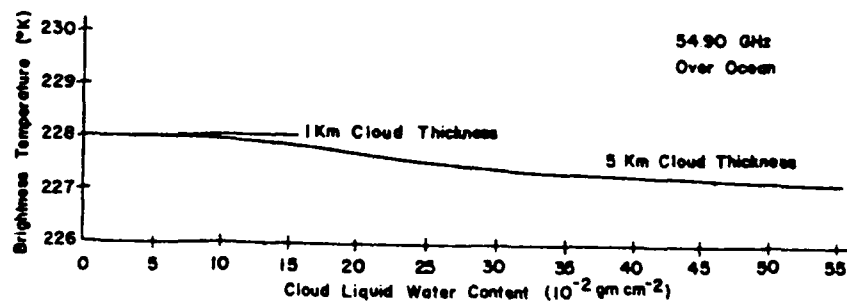


Figure 11. 54.90 GHz brightness temperature as a function of cloud thickness and liquid water content (Mid-Latitude Spring/Fall profile over ocean).

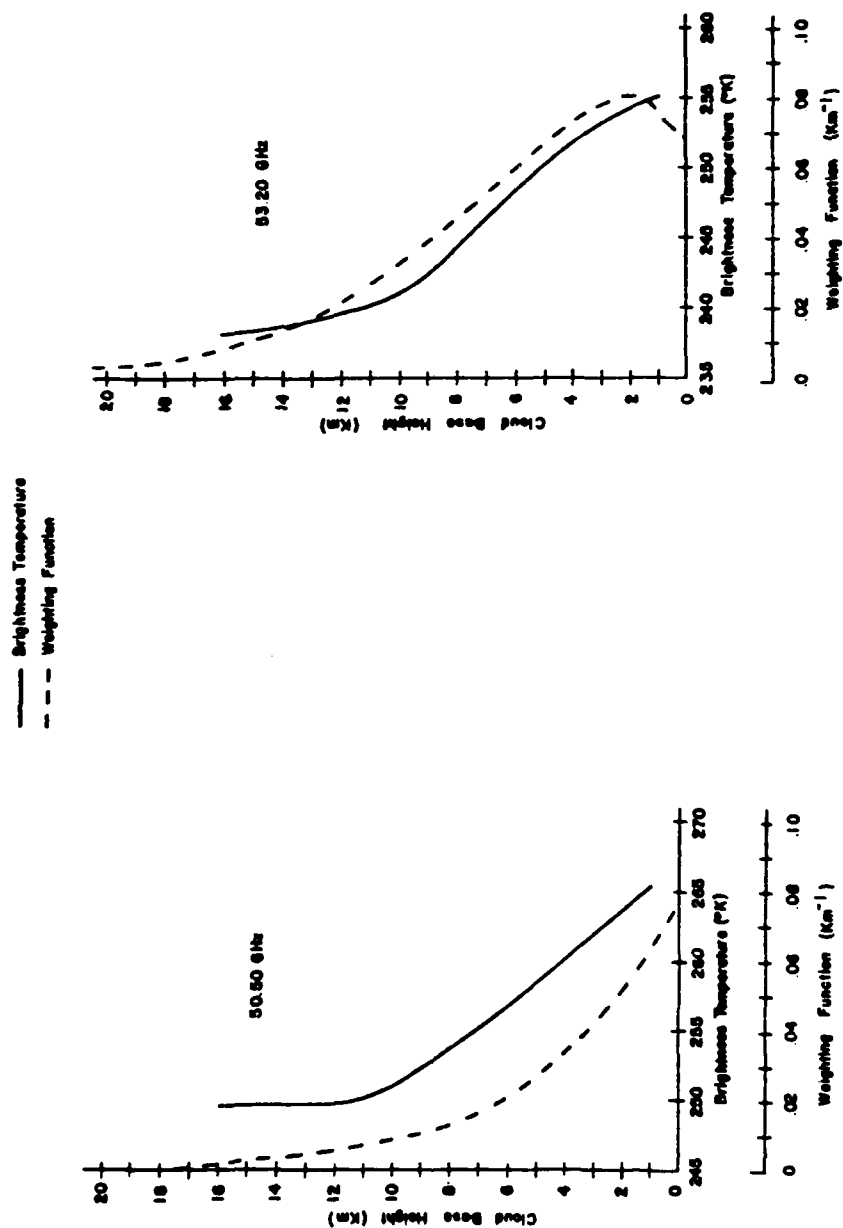


Figure 12. 50.50 GHz brightness temperature dependence on cloud base height for a 2 Km thick Deirmendjian L-Model cloud (Mid-Latitude Spring/Fall profile over land).

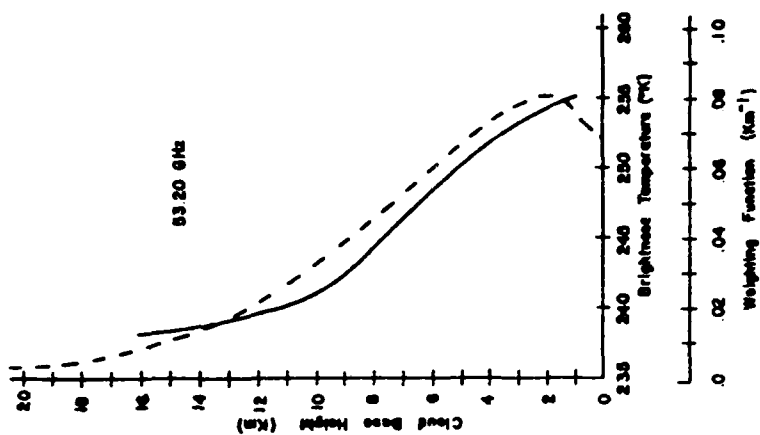


Figure 13. 53.20 GHz brightness temperature dependence on cloud base height for a 2 Km thick Deirmendjian L-Model cloud (Mid-Latitude Spring/Fall profile over land).

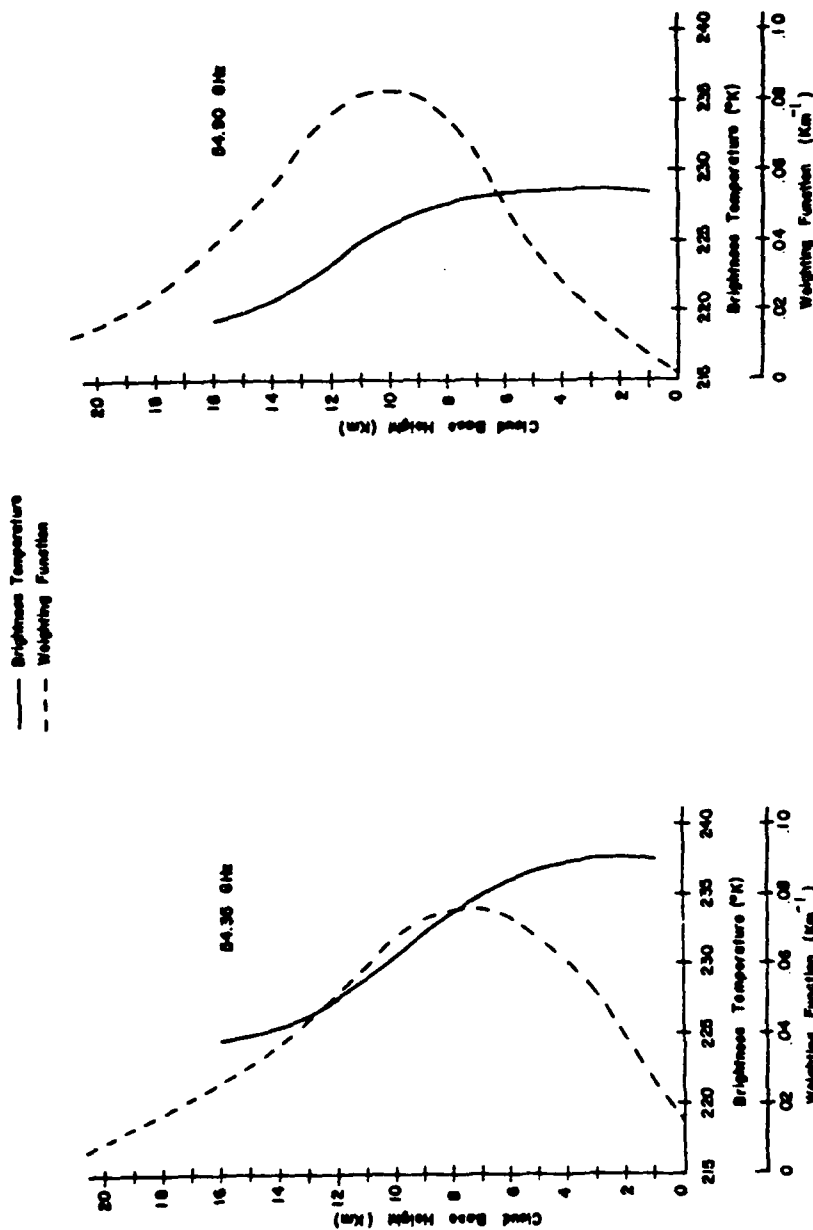


Figure 14. 54.35 GHz brightness temperature dependence on cloud base height for a 2 Km thick Deirmendjian L-Model cloud (Mid-Latitude Spring/Fall profile over land).

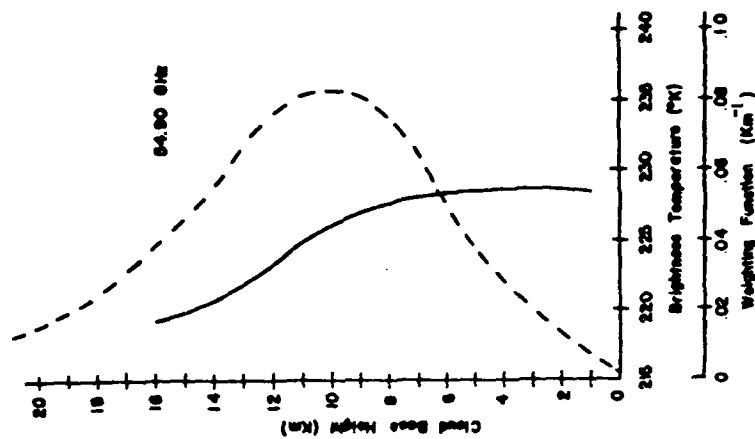


Figure 15. 54.90 GHz brightness temperature dependence on cloud base height for a 2 Km thick Deirmendjian L-Model cloud (Mid-Latitude Spring/Fall profile over land).

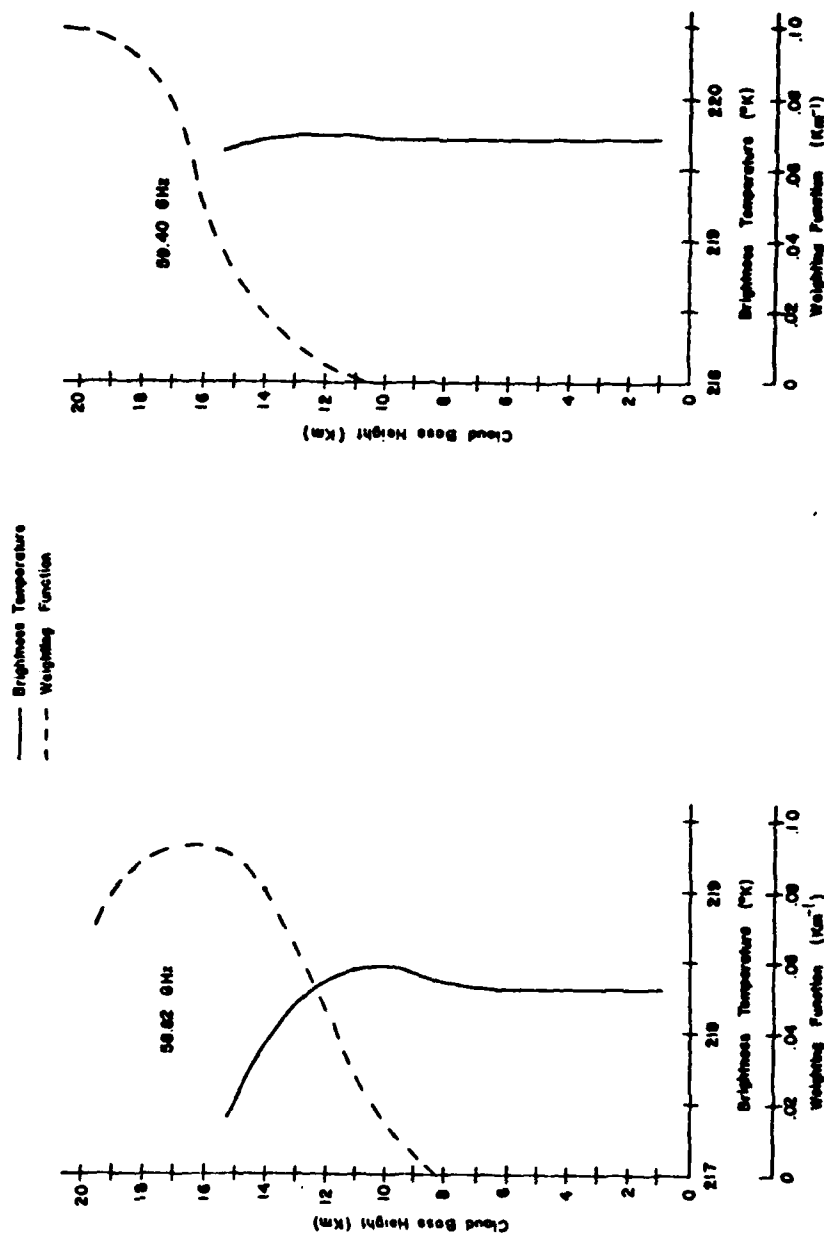


Figure 16. 58.82 GHz brightness temperature dependence on cloud base height for a 2 Km thick Deirmendjian L-Model cloud (Mid-Latitude Spring/Fall profile over land).

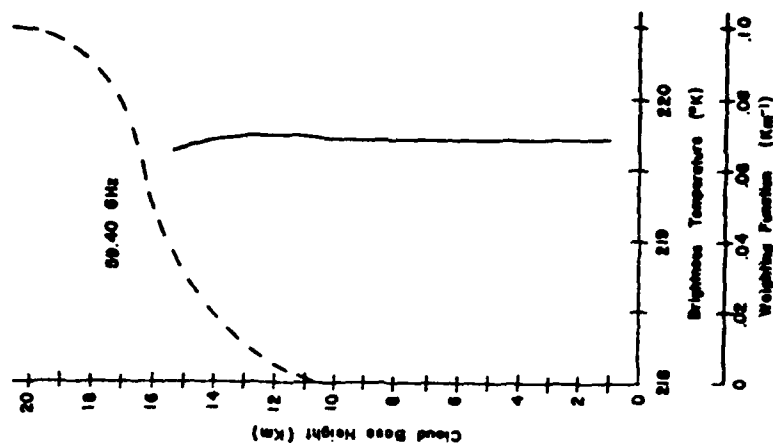


Figure 17. 59.40 GHz brightness temperature dependence on cloud base height for a 2 Km thick Deirmendjian L-Model cloud (Mid-Latitude Spring/Fall profile over land).

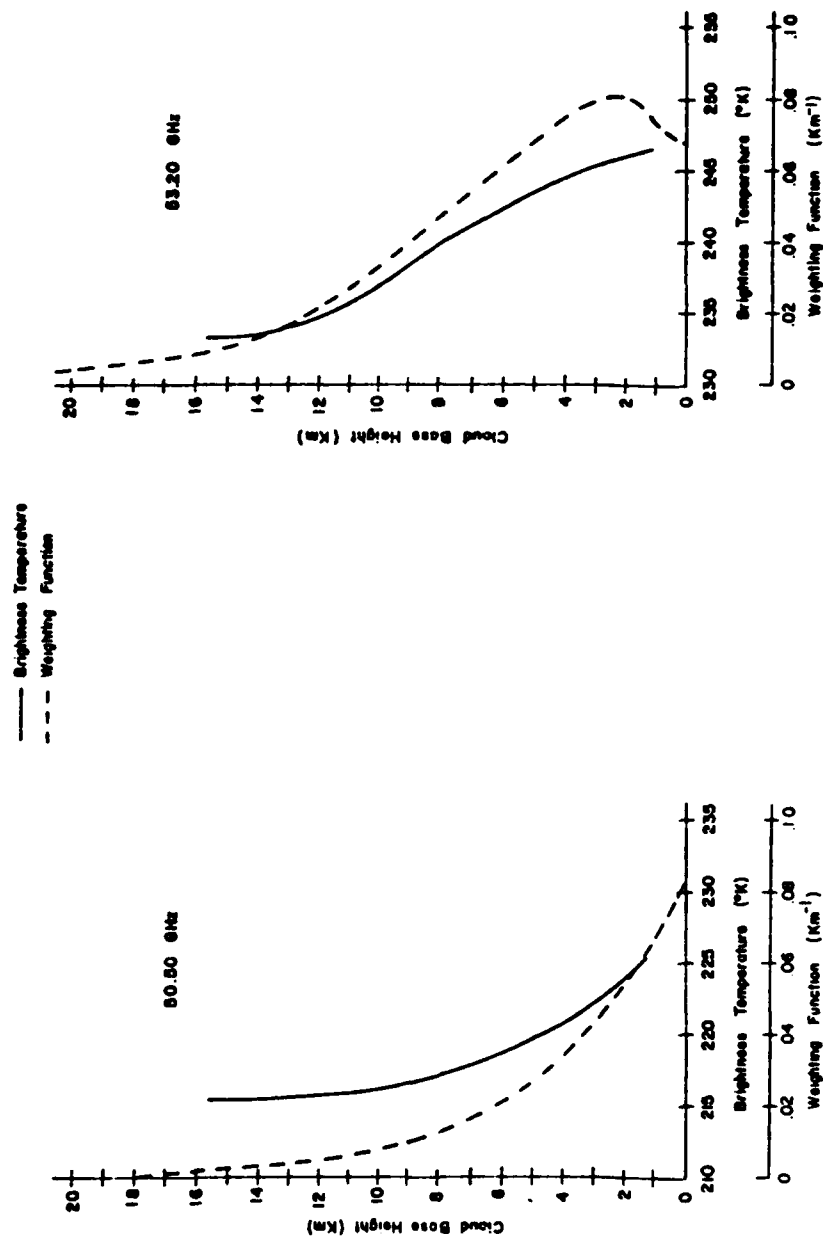


Figure 18. 50.50 GHz brightness temperature dependence on cloud base height for a 2 Km thick Deirmendjian L-Model cloud (Mid-Latitude Spring/Fall profile over ocean).

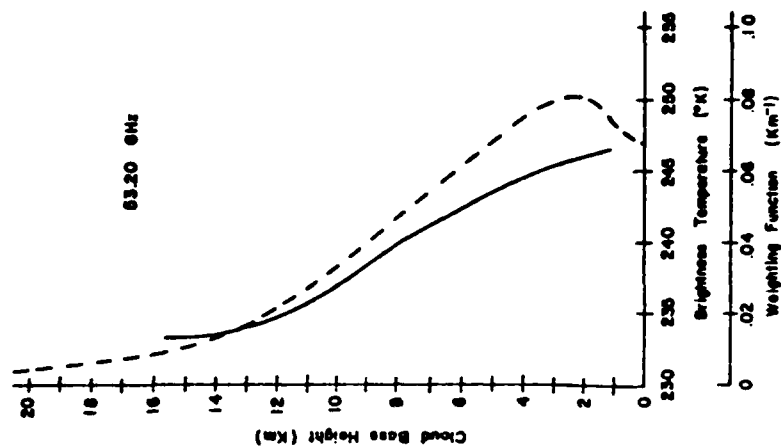


Figure 19. 53.20 GHz brightness temperature dependence on cloud base height for a 2 Km thick Deirmendjian L-Model cloud (Mid-Latitude Spring/Fall profile over ocean).

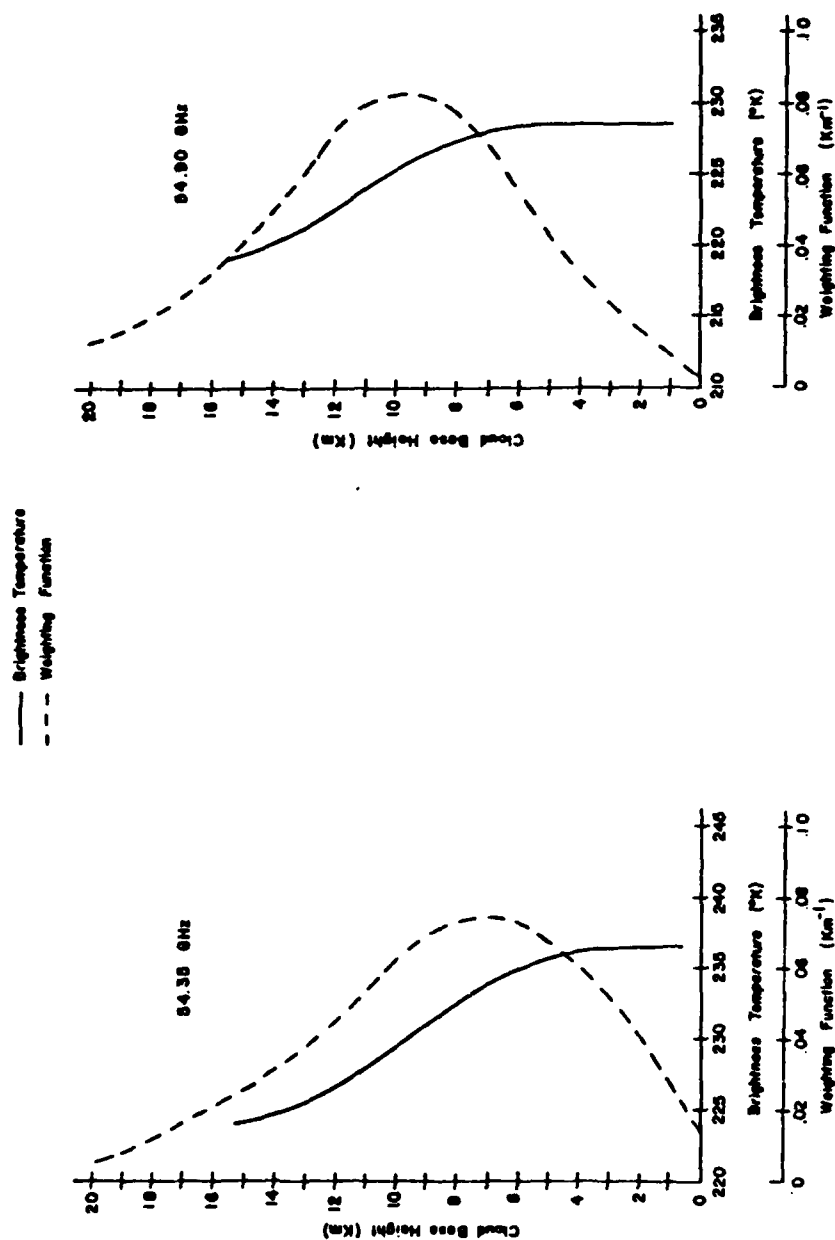


Figure 20. 54.35 GHz brightness temperature dependence on cloud base height for a 2 Km thick Deirmendjian L-Model cloud (Mid-Latitude Spring/Fall profile over ocean).

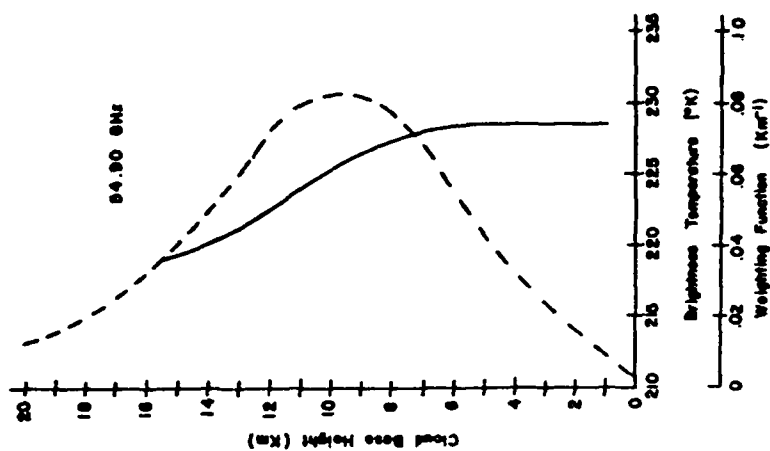


Figure 21. 54.90 GHz brightness temperature dependence on cloud base height for a 2 Km thick Deirmendjian L-Model cloud (Mid-Latitude Spring/Fall profile over ocean).

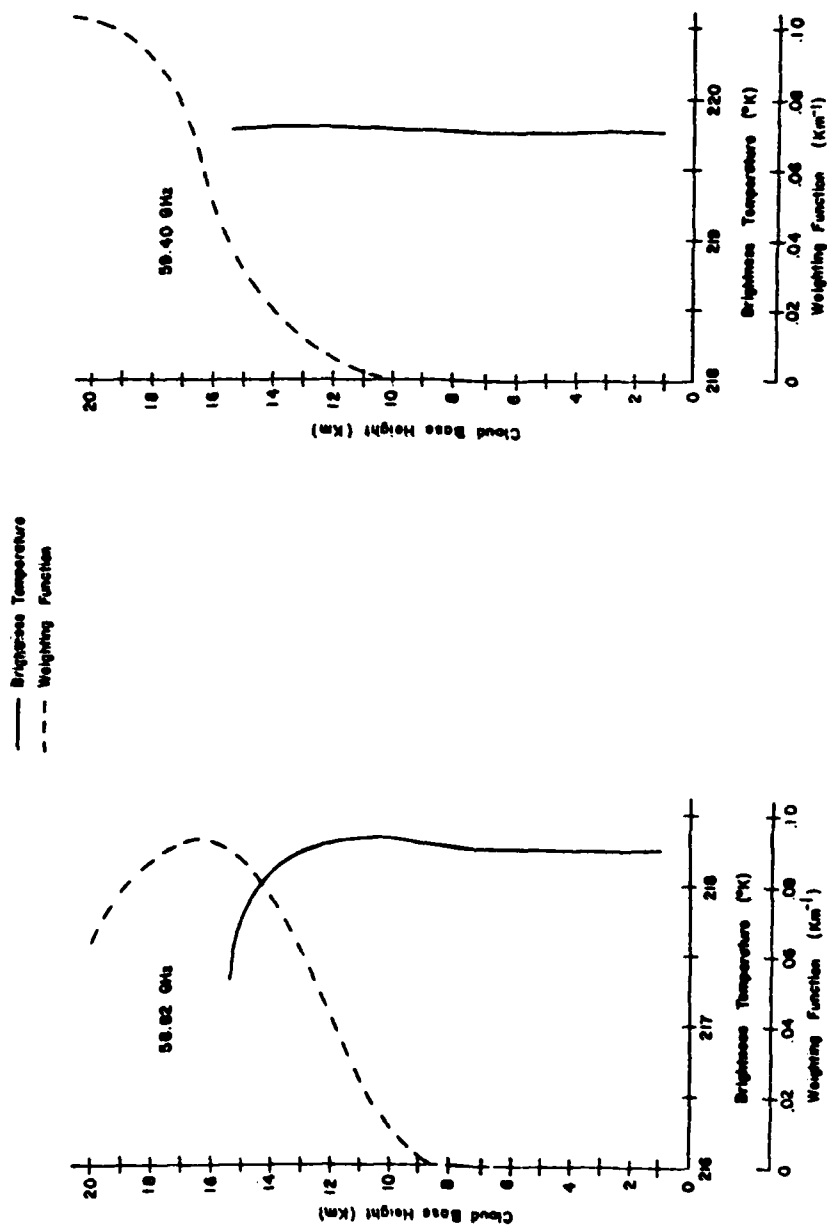


Figure 22. 58.82 GHz brightness temperature dependence on cloud base height for a 2 Km thick Deirmendjian L-Model cloud (Mid-Latitude Spring/Fall profile over ocean).

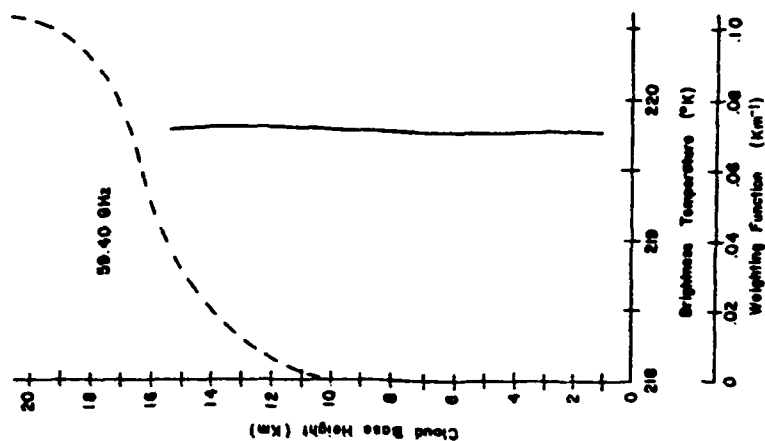


Figure 23. 59.40 GHz brightness temperature dependence on cloud base height for a 2 Km thick Deirmendjian L-Model cloud (Mid-Latitude Spring/Fall profile over ocean).

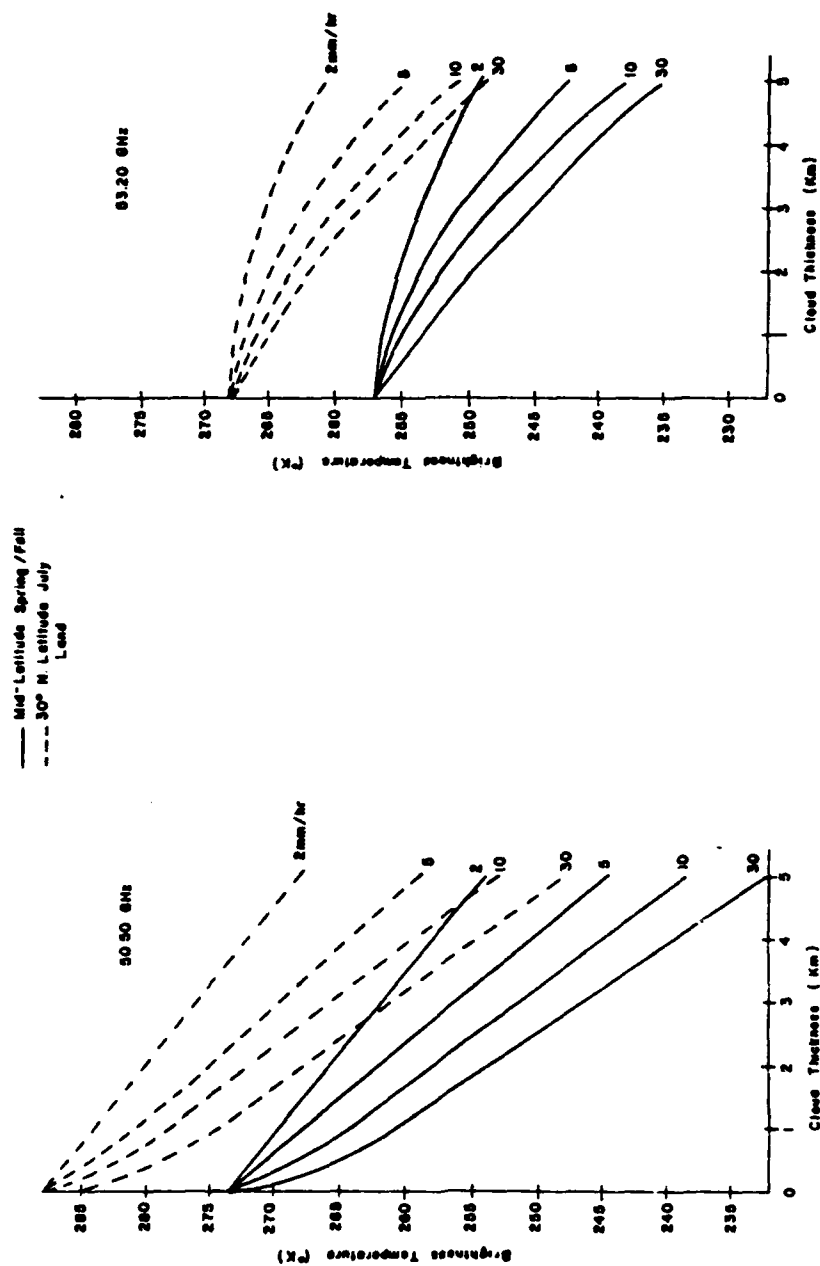


Figure 24. 50.50 GHz channel profile dependence over land.

Figure 25. 53.20 GHz channel profile dependence over land.

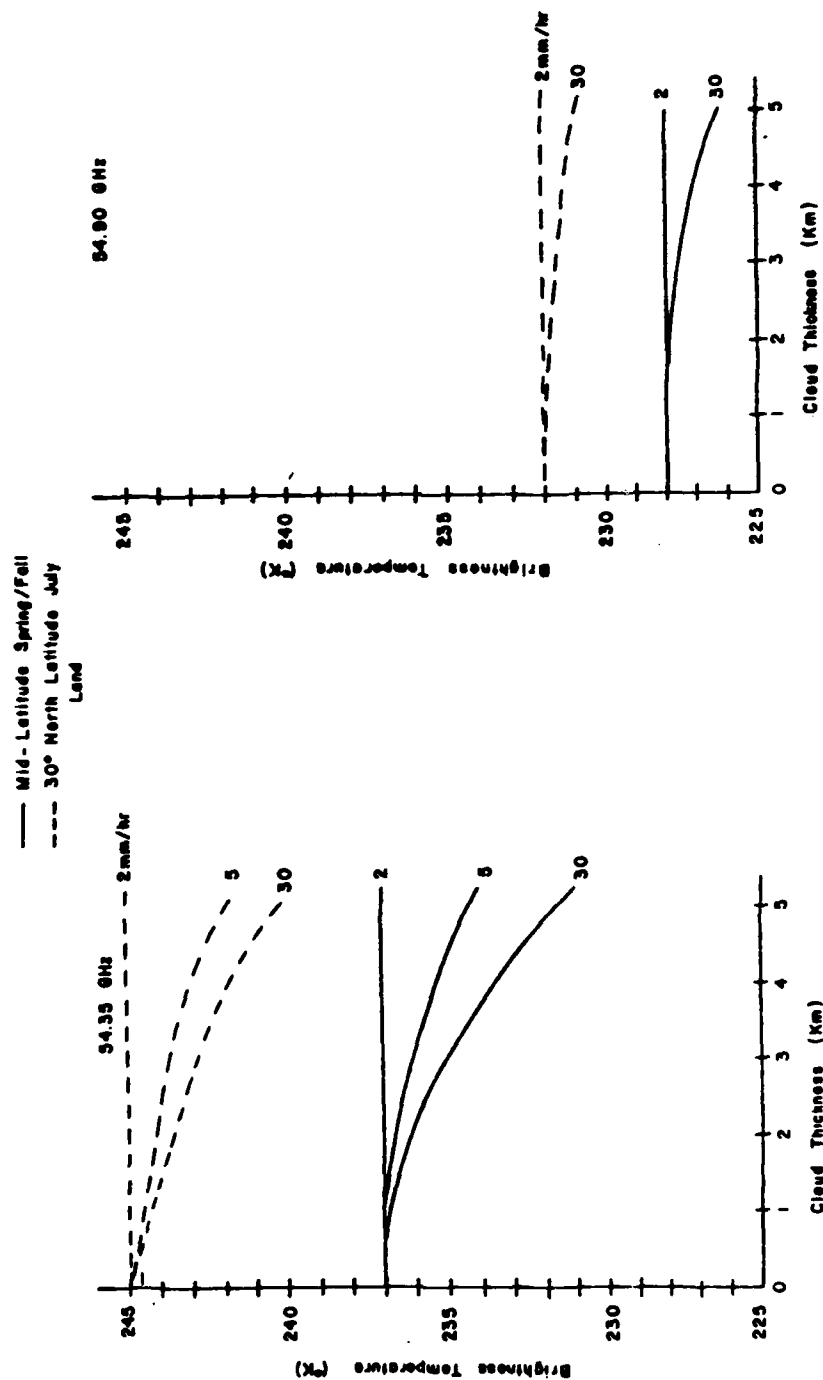


Figure 26. 54.35 GHz channel profile dependence over land.

Figure 27. 54.90 GHz channel profile dependence over land.

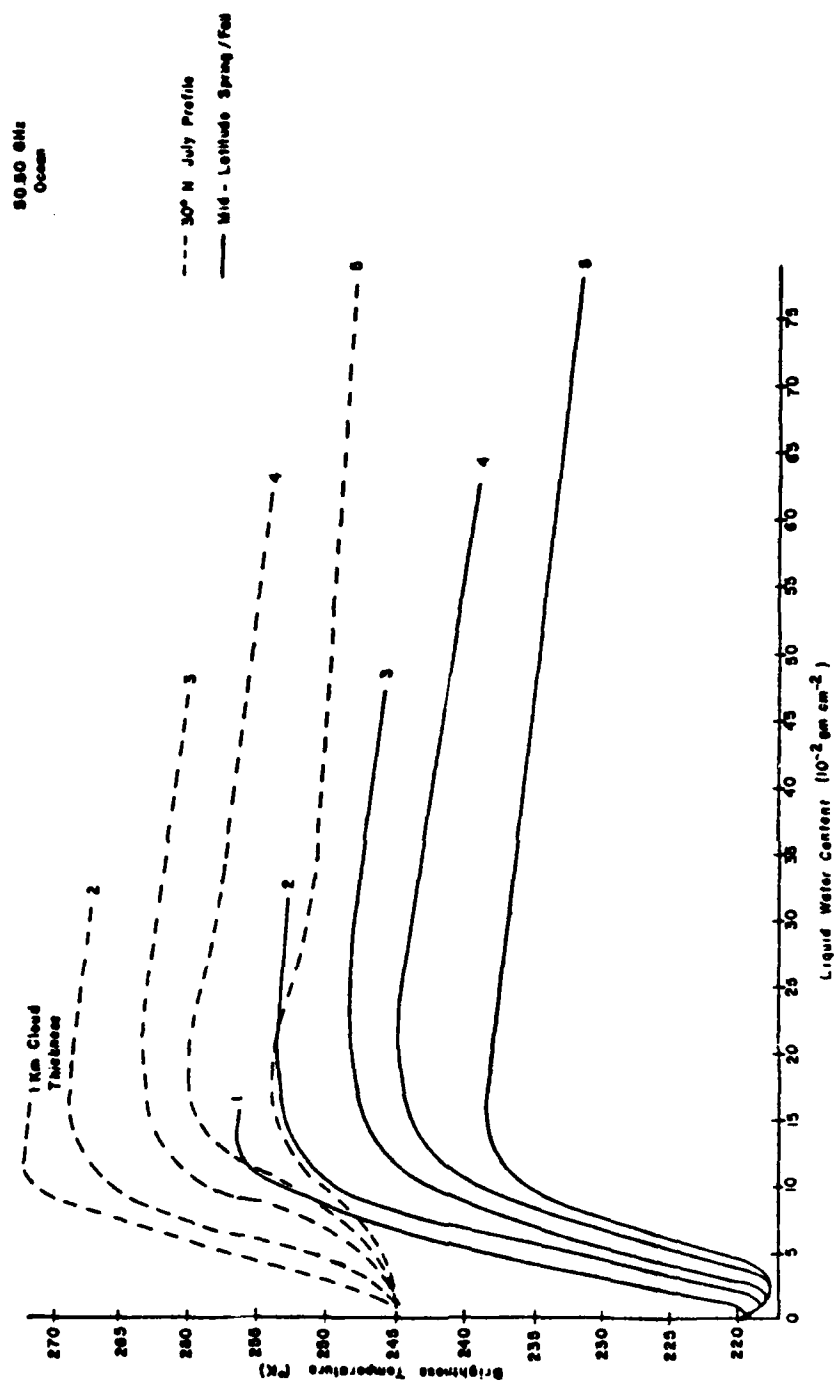


Figure 28. 50.50 GHz channel profile dependence over ocean.

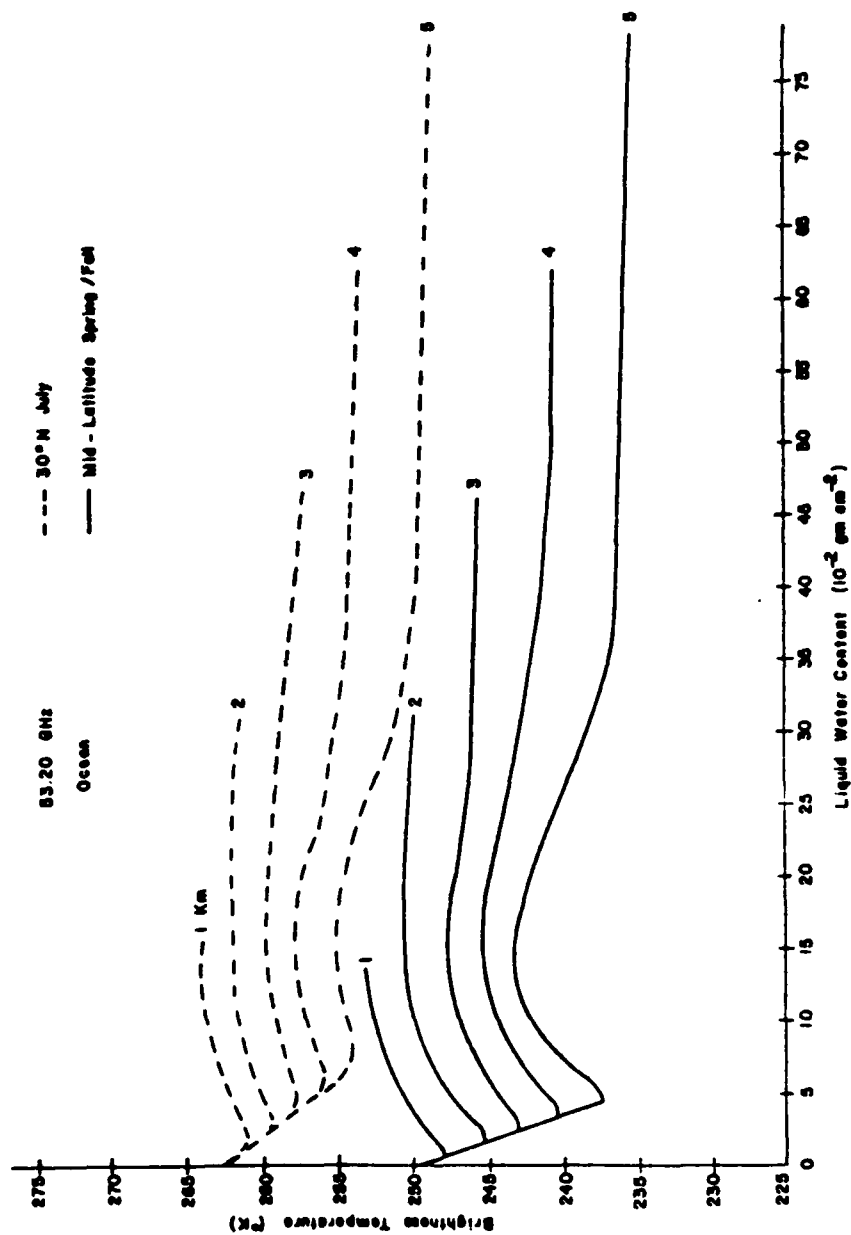


Figure 29. 53.20 GHz channel profile dependence over ocean.

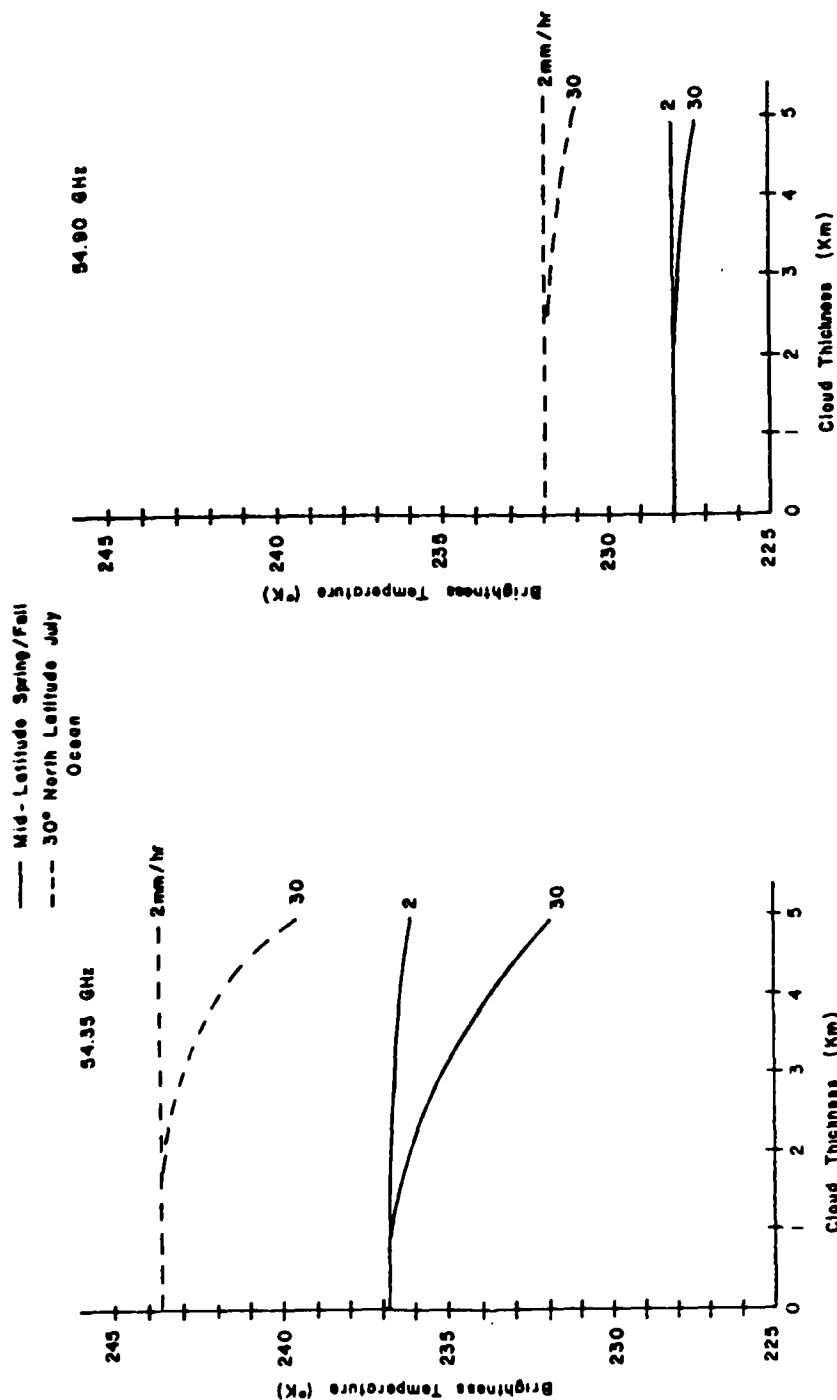


Figure 30. 54.35 GHz channel profile dependence over ocean.

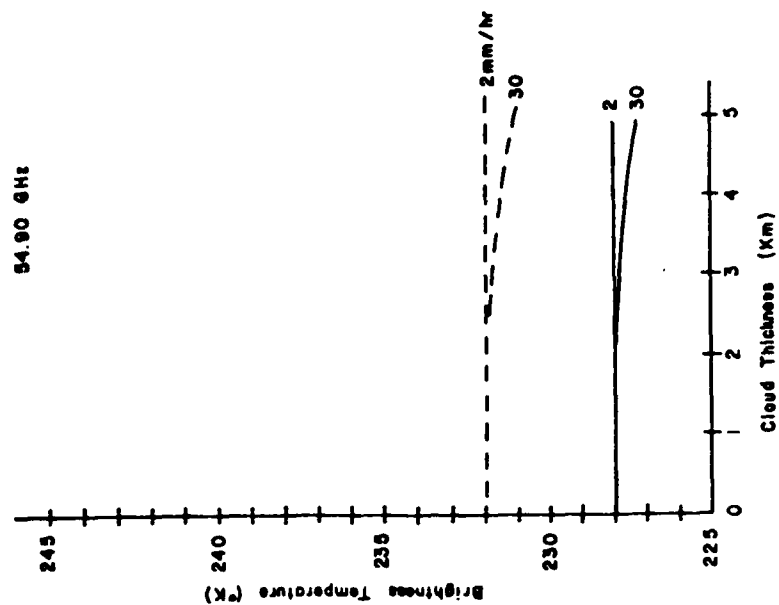


Figure 31. 54.90 GHz channel profile dependence over ocean.

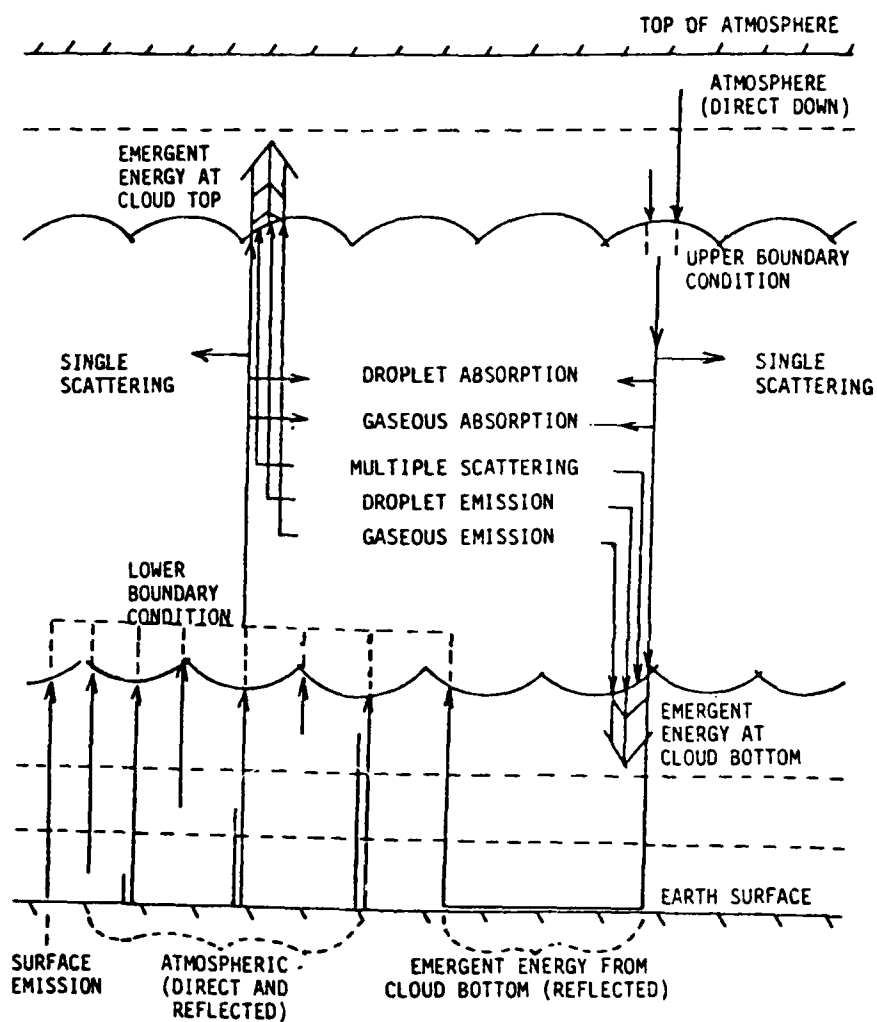


Figure 32. Radiative transfer through a cloud layer.

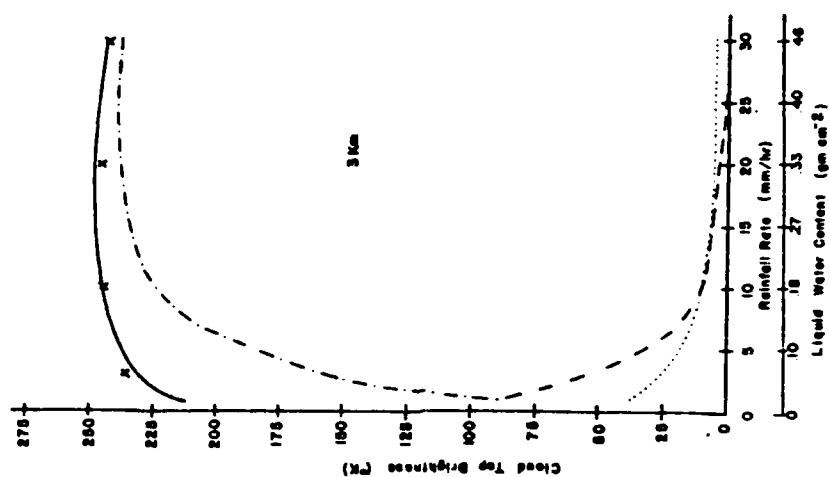


Figure 33. Component contributions to 50.50 GHz cloud top brightness for a 1 Km thick cloud over ocean (Mid-Latitude Spring/Fall profile).

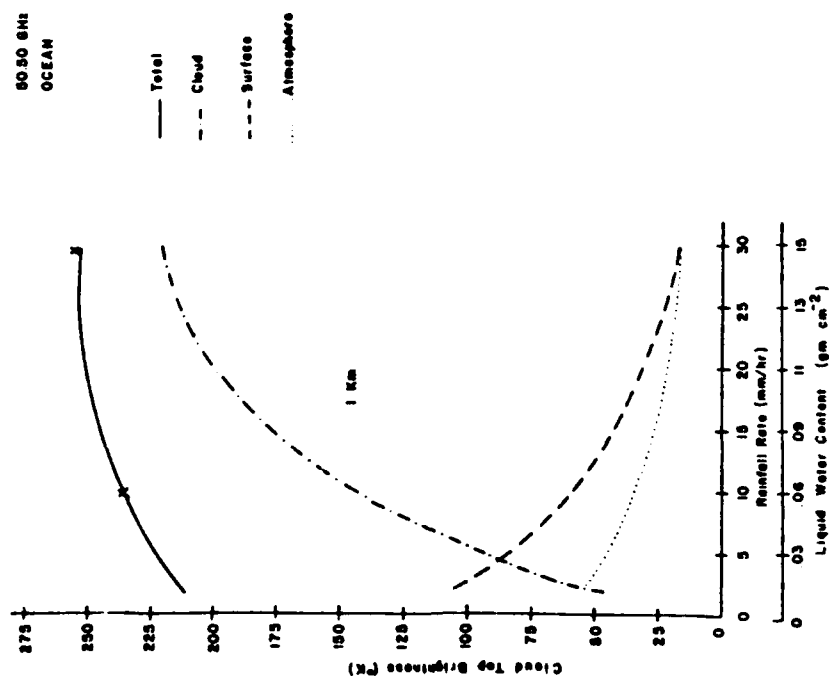


Figure 34. Component contributions to 50.50 GHz cloud top brightness for a 3 Km thick cloud over ocean (Mid-Latitude Spring/Fall profile).

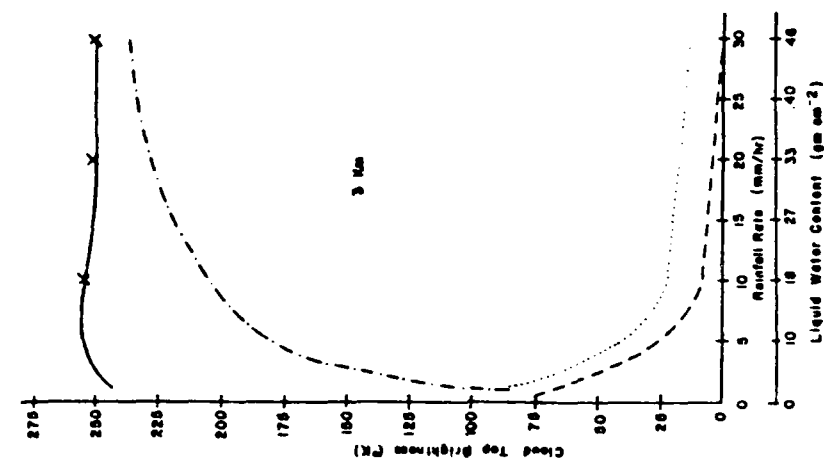


Figure 35. Component contributions to 53.20 GHz cloud top brightness for a 1 km thick cloud over ocean (Mid-Latitude Spring/Fall profile).

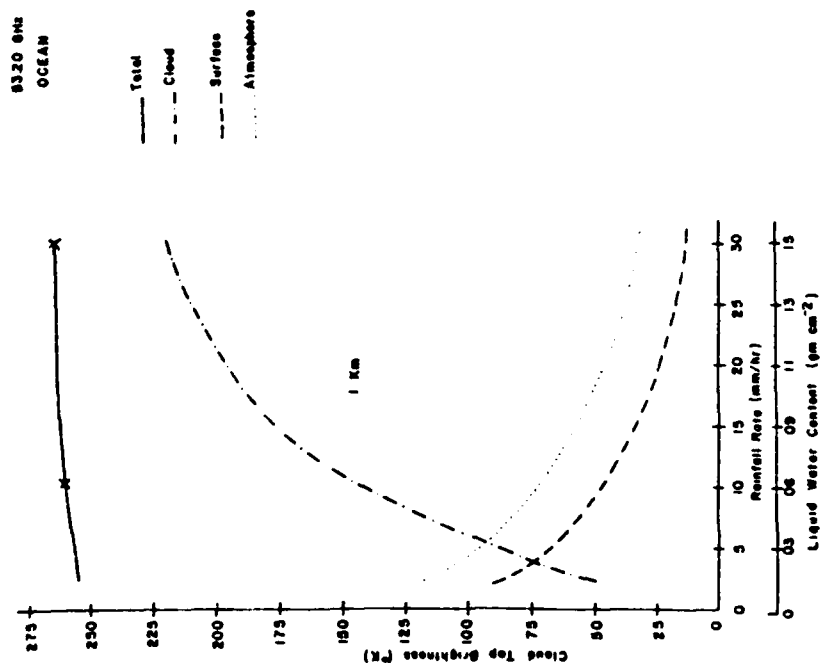


Figure 36. Component contributions to 53.20 GHz cloud top brightness for a 3 Km thick cloud over ocean (Mid-Latitude Spring/Fall profile).

CHAPTER 6

TEMPERATURE RETRIEVAL

The difficulty in reconstructing a temperature profile from radiance or brightness temperature values is due to the fact that the Fredholm equation with fixed limits may not always have a solution for an arbitrary function. The extraction of $T(z)$ from under the integration sign of Equation (4-19) is possible because for certain frequency ranges the integrand reaches a strong maximum at different heights.

6.1 AFGWC Statistical Method

The SSM/T retrieval method is based on a linear multiple regression technique. It is assumed that the deviation of the parameter vector (temperature profile) from the climatological mean may be expressed as a linear combination of the deviations of measured data (brightness temperatures) from its mean. Thus:

$$\hat{p} - \langle p \rangle = D(d - \langle d \rangle) \quad (6-1)$$

where p is the atmospheric temperature vector, \hat{p} is the predicted value of p , $\langle p \rangle$ is the climatological mean of p , d is the data vector of brightness temperatures, $\langle d \rangle$ is the vector of brightness temperature mean values, and D is a matrix. The D -matrix is determined by the condition that the square of the difference between the true value of the vector p and the predicted value, \hat{p} , be a minimum. This leads to the equation:

$$D = C(p-\langle p \rangle, d-\langle d \rangle) C^{-1}(d-\langle d \rangle, d-\langle d \rangle) \quad (6-2)$$

where $C(.,.)$ denotes the covariance matrix of two arguments. Eq. (6-1) can be written as:

$$\hat{p} = Dd + A \quad (6-3a)$$

where

$$A = \langle p \rangle - D\langle d \rangle \quad (6-3b)$$

so that the predicted value of the temperature vector is expressed as a constant, A , and a linear combination of the data.

The covariance matrix, C , required in Eq. (6-2) has been determined from apriori data for implementation purposes. That is, the microwave response for a large number of archived atmospheres representing a wide range of meteorological conditions was calculated, and from this information the D -matrices were determined. After implementation, real time data will be used to update these D -matrices on a regular bases.

Since microwave radiometers possess inherent instrumental noise, this noise must be accounted for in the computations. The data vector, d , may be written as:

$$d = d_0 + \delta \quad (6-4)$$

where d_0 is the exact brightness value and δ is a random error representing system noise. Then,

$$C(p-\langle p \rangle, d-\langle d \rangle) = C(p-\langle p \rangle, d_0-\langle d_0 \rangle) \quad (6-5)$$

and

$$C(d-\langle d \rangle, d-\langle d \rangle) = C(d_0-\langle d_0 \rangle, d_0-\langle d_0 \rangle) + C(\delta, \delta) \quad (6-6)$$

Eq. (6-6) incorporates the instrumental noise characteristics in the computations through the noise covariance matrix, $C(\delta, \delta)$.

Eq. (4-29) may be rewritten to represent clear column brightness at the top of the atmosphere as:

$$\begin{aligned} T_B(\nu, \infty; \mu_i) &= \epsilon_\nu T_s \tau_\nu(0, \infty; \mu_i) + \int_0^\infty T(z) d\tau_\nu(z, \infty; \mu_i) \\ &+ (1 - \epsilon_\nu) \tau_\nu(0, \infty; \mu_i) \left[\int_0^\infty T(z) d\tau_\nu(0, z; -\mu_i) \right]. \end{aligned} \quad (6-7)$$

Rewriting Eq. (6-7) to obtain an expression for $\epsilon_\nu T_s$ yields:

$$\begin{aligned} \epsilon_\nu T_s &= [T_B(\nu, \infty; \mu_i) - \tau_\nu(0, \infty; \mu_i)(1 - \epsilon_\nu) \int_0^\infty T(z) d\tau_\nu(0, z; -\mu_i) \\ &- \int_0^\infty T(z) d\tau_\nu(z, \infty; \mu_i)] / \tau_\nu(0, \infty; \mu_i) \end{aligned} \quad (6-8)$$

Now defining:

$$T_{sky} = \int_0^\infty T(z) d\tau_\nu(0, z; -\mu_i) ,$$

$$T_{atm} = \int_0^\infty T(z) d\tau_\nu(z, \infty; \mu_i) ,$$

and

$$T_B(\nu) = T_B(\nu, \infty; \mu_i) ;$$

Eq. (6-8) may be expressed more simply as:

$$\epsilon_\nu T_s = [T_B(\nu) - \tau_\nu(0, \infty; \mu_i)(1 - \epsilon_\nu) T_{sky} - T_{atm}] / \tau_\nu(0, \infty; \mu_i) .$$

Then

$$\epsilon_v T_s \tau_v(0, \infty; \mu_i) \left(1 - \frac{T_{sky}}{T_s}\right) = [T_B(v) - \tau_v(0, \infty; \mu_i) T_{sky} - T_{atm}]$$

and

$$\epsilon_v T_s = [T_B(v) - \tau_v(0, \infty; \mu_i) T_{sky} - T_{atm}] / [\tau_v(0, \infty; \mu_i) \left(1 - \frac{T_{sky}}{T_s}\right)] \quad (6-9)$$

In particular,

$$(\epsilon_v T_s)_{50.5} = [T_B(v) - \tau_v(0, \infty; \mu_i) T_{sky} - T_{atm}]_{50.5} / [\tau_v(0, \infty; \mu_i) \left(1 - \frac{T_{sky}}{T_s}\right)]_{50.5} \quad (6-10)$$

Eq. (6-10) is used to obtain an expression for $\tau_v T_s$ in terms of the channel 1 brightness.

For DMSP application a data vector was chosen to be dependent only on atmospheric conditions. That is:

$$d_i = \tau_v(0, \infty) T_{sky} + T_{atm} \quad (6-11)$$

From Eq. (6-9) we may write:

$$\tau_v(0, \infty; \mu_i) T_{sky} + T_{atm} = T_B(v) - \epsilon_v T_s \tau_v(0, \infty; \mu_i) \left(1 - \frac{T_{sky}}{T_s}\right) = d_i \quad (6-12)$$

Since the terms on the left are clearly atmospheric dependent only, the correction to brightness temperature represented by the negative term on the right will clearly remove the effects of surface emission and reflection from the brightness value. Substituting Eq. (6-10) into Eq. (6-12) yields:

$$d_i = T_B(v) - [T_B(50.5) - S_{50.5}] a_{v_i} \quad (i=1, 2, \dots, 6) \quad (6-13)$$

where

$$s_{50.5} = [\tau_v(0, \infty; \mu_i) T_{sky} + T_{atm}]_{50.5}$$

and

$$a_{v_i} = \frac{[\tau_v(0, \infty; \mu_i)(1 - \frac{T_{sky}}{T_s})]_{v_i}}{[\tau_v(0, \infty; \mu_i)(1 - \frac{T_{sky}}{T_s})]_{50.5}}$$

The values for $s_{50.5}$ and the a_{v_i} have been computed for implimentation from the same apriori data used to compute the D-matrices. Then the multiple regression Equations (6-3a) and (6-3b) may be expressed as:

$$\hat{p} = ST_B + A' \quad (6-14a)$$

and

$$A' = \langle p \rangle - D \langle d \rangle + s_{50.5} D a \quad (6-14b)$$

where

$$T_B = \begin{pmatrix} T_{50.5} \\ \vdots \\ T_{59.4} \end{pmatrix}$$

and $S = (-Da : D)$ is a matrix whose first column is $-Da$ and whose remaining columns are the columns of D .

6.2 Chahine's Relaxation Method

As a consequence of the mean value theorem, the contribution to brightness temperature due to atmospheric emission can be expressed as the change in upwelling brightness at one level, z_j (the level where the channel weighting function peaks), times the effective width of the

weighting function, $\Delta_j z$. Then

$$T_B(v_j, \infty) - T_{S\varepsilon_v\tau_v}(0, \infty) = T(z_j) \left[\frac{\partial \tau_v(z, \infty)}{\partial z} \right]_{z_j} \Delta_j z \quad (6-15)$$

where T_S and $T(z_j)$ are the true temperature values and $T_B(v_j, \infty)$ is the observed brightness temperature. If we arbitrarily guess a temperature profile, then the calculated brightness temperature can be represented as:

$$T'_B(v_j, \infty) - T'_{S\varepsilon_v\tau'_v}(0, \infty) = T'(z_j) \left[\frac{\partial \tau'_v(z, \infty)}{\partial z} \right]_{z'_j} \Delta'_j z \quad (6-16)$$

Dividing Eq. (6-15) by Eq. (6-16) yields:

$$\frac{T_B(v_j, \infty) - T_{S\varepsilon_v\tau_v}(0, \infty)}{T'_B(v_j, \infty) - T'_{S\varepsilon_v\tau'_v}(0, \infty)} = \frac{T(z_j) \left[\frac{\partial \tau_v(z, \infty)}{\partial z} \right]_{z_j} \Delta_j z}{T'(z_j) \left[\frac{\partial \tau'_v(z, \infty)}{\partial z} \right]_{z'_j} \Delta'_j z} \quad (6-17)$$

Since the transmissivities and weighting function values do not change very much as a function of temperature,

$$\frac{\left[\frac{\partial \tau_v(z, \infty)}{\partial z} \right]_{z_j} \Delta_j z}{\left[\frac{\partial \tau'_v(z, \infty)}{\partial z} \right]_{z'_j} \Delta'_j z} = 1$$

Therefore,

$$\frac{T'(z) [T_B(v_j, \infty) - T_{S\varepsilon_v\tau_v}(0, \infty)]}{[T'_B(v_j, \infty) - T'_{S\varepsilon_v\tau'_v}(0, \infty)]} = T(z) \quad (6-18)$$

When the contribution to brightness temperature at the top of the atmosphere due to the surface emission term is dominate or negligible,

we obtain the relaxation equation of Chahine:

$$\frac{T'(z)T_B(\nu_j, \infty)}{T_B'(\nu_j, \infty)} = T(z) \quad (6-19)$$

The iterative method of solving for the correct temperature values corresponding to the peak levels for the weighting functions of j channels is as follows:

- 1) Make an initial guess ($n=0$) for the $T^n(z_j)$, where the superscript denotes iteration number.
- 2) Interpolate temperature values, $T^n(z_k)$, to N standard levels from the $T^n(z_j)$.
- 3) Using an accurate quadrature formula, evaluate the corresponding brightness temperature values, $T_B(\nu_j, \infty)$ using Eq. (4-17).
- 4) Compare the computed brightness temperatures with the observed values, $\tilde{T}_B(\nu_j, \infty)$. If the residuals,

$$R_j^n = |\tilde{T}_B(\nu_j, \infty) - T_B(\nu_j, \infty)| / \tilde{T}_B(\nu_j, \infty),$$

are less than σ ($\sigma \rightarrow 0$) for each channel, then $T^n(z_k)$ is a solution.

- 5) If any of the residuals are greater than σ , then Eq. (6-19) is applied to each channel to obtain a new estimate of the temperature for the level corresponding to the peak of the weighting function for each channel.

- 6) Go back to step 2) and repeat until all residuals are less than σ .

6.3 Presentation of Results

The two retrieval methods described in Sections 6.1 and 6.2 were

used to retrieve the Mid-Latitude Spring/Fall profile used in this sensitivity study. The results of these retrievals are depicted in Figures 37 through 40. In each case the curve labeled (a) is the actual profile used to calculate the brightness temperatures. The curve labeled (b) is the retrieval accomplished using clear column brightness temperature values. Curves labeled (c) through (f) represent precipitating cloud cases of increasing rainfall rates and thicknesses.

Figure 37 and 38 indicate that the AFGWC method has very successfully removed surface effects from the retrieval. Note how similar the retrieved profiles are over land and over ocean for the same thickness and rainfall rate. Curve (c) on both figures represents a light to moderate precipitation case (up to 5 mm/hr and 2 Km thickness). The surface temperature suffers some degradation from the clear column case but still stays within 10°K of truth. Above 3 Km the retrieval for all levels is within .5°K of the clear column retrieval. This indicates that for light to moderate rain and certainly for nonprecipitating cloudy atmospheres, the AFGWC method will provide a global data base of atmospheric temperature profiles representing a substantial improvement over climatology. The method does perform significantly worse for heavier rainfall rates and thicker clouds. The worst errors occur at the surface and near the tropopause. Rainfall rates of this magnitude (greater than 5 mm/hr) do not occur over very large areas or for very long time periods. Therefore, they should not have a significant effect on global mapping, although they do point out the need for careful quality control of individual profiles.

Figures 39 and 40 indicate that Chahine's relaxation method performs very well below the tropopause for clear atmospheric conditions.

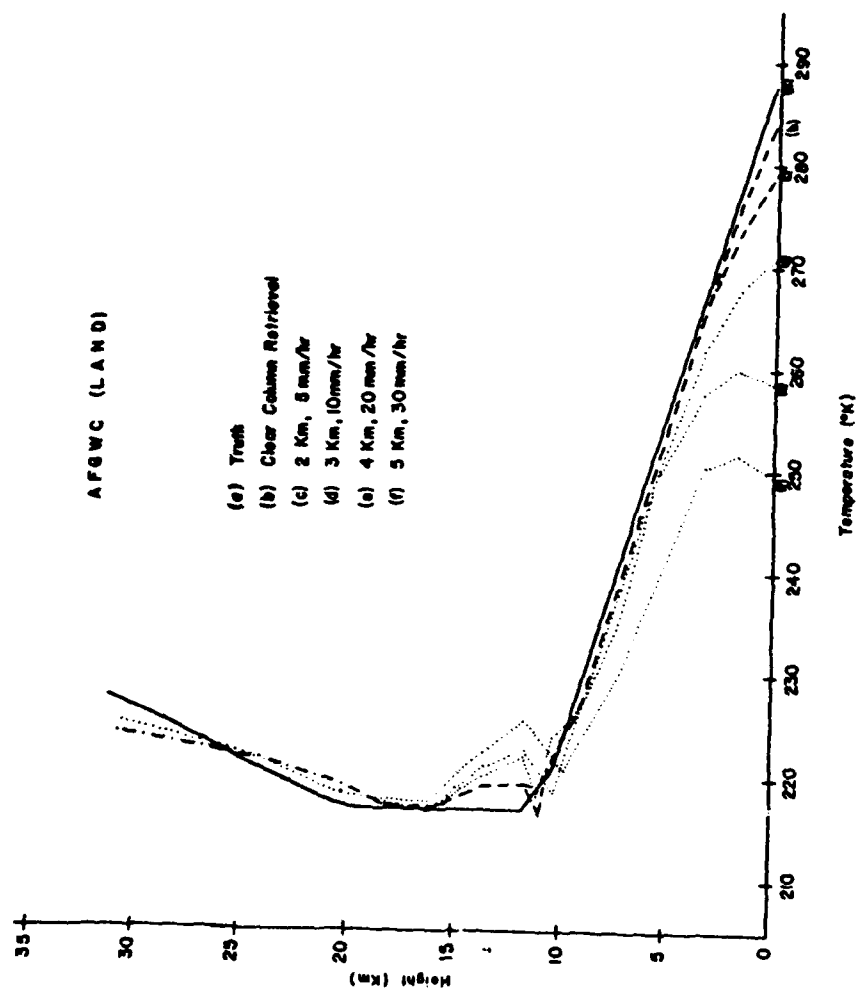


Figure 37. AFGWC temperature retrieval over land (Mid-Latitude Spring/Fall profile).

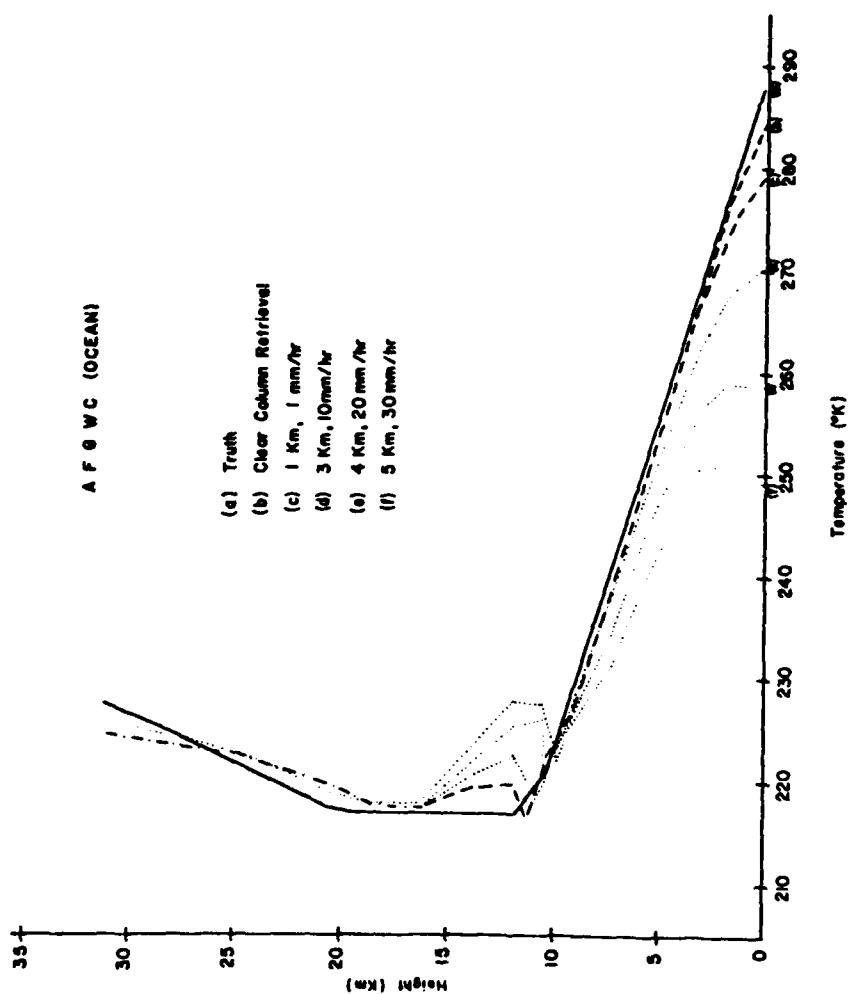


Figure 38. AFGWC temperature retrieval over ocean (Mid-Latitude Spring/Fall profile).

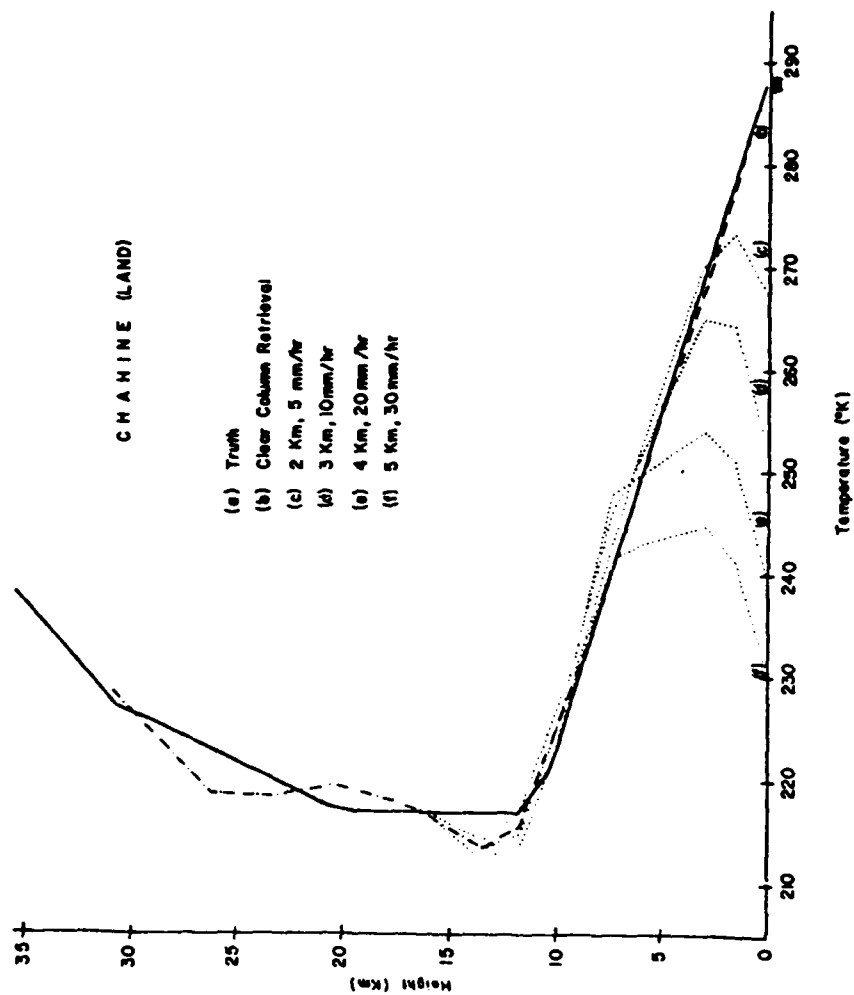


Figure 39. Chahine temperature retrieval over land (Mid-Latitude Spring/Fall profile).

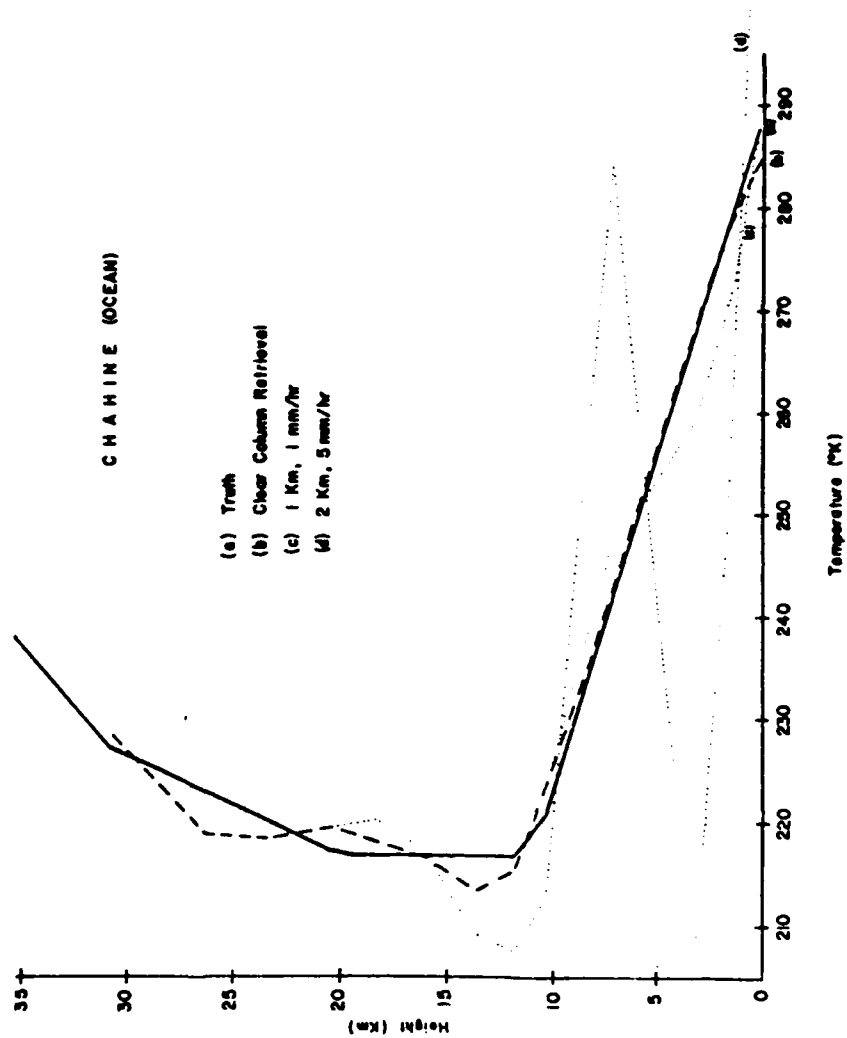


Figure 40. Chahine temperature retrieval over ocean (Mid-Latitude Spring/Fall profile).

Over land the surface temperature becomes poor very rapidly for even moderate precipitating conditions. For a 2 Km thick cloud with a precipitation rate of 5 mm/hr the retrieved surface temperature is 19°K too low. The quality of the retrieved temperature profile continues to degenerate rapidly as the degree of precipitation increases.

Over the ocean Chahine's method continues to do well for clear atmospheric conditions. At a rainfall rate of 1 mm/hr with a 1 Km thick cloud, the temperature retrieval begins to worsen in the lower troposphere, although the surface temperature retrieved is good. For a 2 Km thick cloud and a 5 mm/hr rainfall rate, this method fails completely, with the retrieved profile oscillating wildly about the truth.

CHAPTER 7

CONCLUSION

Channels 1, 2, 3 and 4 of the SSM/T have been shown to be effected by precipitation to various degrees.

For channels 3 and 4 the effects are quite small and in fact are of an order close to that of the instrument noise level. In other words, the variations noted for these channels are basically insignificant to operational applications.

Channels 1 and 2 display a much more significant response to precipitation. General trends in the brightness variations for these channels are dependent on cloud liquid water content, thickness and surface emissivity.

For a theoretical retrieval scheme based on the premise that the input brightness temperature values are clear column values, these variations cause a rapid degradation in the accuracy of the retrieved temperature profile. However, methods are available, such as the AFGWC statistical method, which can somewhat adjust to surface and lower tropospheric conditons. When clear column conditions exist, the retrieval can be made without degradation due to surface emissivity. For precipitating conditions, the surface emissivity is underestimated, but this error tends to compensate for extinction within the precipitation layer reducing the brightness error in channels sensing the lower troposphere. Although, very high rainfall rates can result in a very poor temperature retrieval, the frequency and spatial coverage of such

AD-A107 962

AIR FORCE INST OF TECH WRIGHT-PATTERSON AFB OH
EFFECTS OF PRECIPITATING AND NONPRECIPITATING CLOUD LAYERS ON T--ETC(U)
JUN 79 P T NIPKO
AFIT-CI-79-282T-S

F/6 4/2

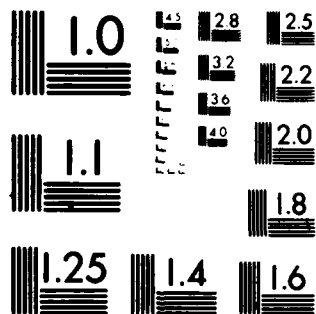
UNCLASSIFIED

NL

212
AD-A107 962



END
DATE
FILMED
-82
NTIC



MICROCOPY RESOLUTION TEST CHART
NATIONAL BUREAU OF STANDARDS 1963-A

atmospheric conditions are sufficiently low that global mapping of vertical temperature profiles derived from microwave sensing from satellite will provide a significant improvement over climatology for forecast model initializations.

REFERENCES

- Chahine, M. T., 1970: Inverse problems in radiative transfer: Determination of atmospheric parameters. J. Atmos. Sci., 27, 960-967.
- _____, 1974: Remote sounding of cloudy atmospheres, I. The single cloud layer. J. Atmos. Sci., 31, 233-243.
- Chandrasekhar, S., 1950: Radiative Transfer. New York, Dover Publications, Inc., 393.
- Deirmendjian, D., 1969: Electromagnetic Scattering on Spherical Polydispersions. New York, Elsevier Press, 75-78.
- Feddes, R. G. and K. N. Liou, 1977: Sensitivity of upwelling radiance in Nimbus 6 HIRS channels to multilayered clouds. J. Atmos. Sci. 82, 5977-5989.
- Hollinger, J. P., 1973: Microwave Properties of a Calm Sea. Naval Research Laboratory Report No. 7110-2, Washington, D.C., 69.
- Kaplan, L. D., 1959: Inference of atmospheric structure from remote radiation measurements. J. Opt., Soc. Amer., 49, 1004-1007.
- King, J. I. F., 1956: The radiative heat transfer of planet earth. Scientific Uses of Earth Satellites, University of Michigan Press, 133-136.
- Liou, K. N., 1975: Applications of the discrete-ordinate method for radiative transfer to inhomogeneous aerosol atmospheres. J. Atmos. Sci., 80, 3434-3440.
- _____, and J. E. Hansen, 1971: Intensity and polarization for single scattering by polydisperse spheres: A comparison of ray optics and Mie theory. J. Atmos. Sci., 28, 995-1004.
- Marshall, J. S. and W. M. Palmer, 1948: The distribution of raindrops with size. J. Meteor., 5, 165-166.
- Meeks, M. L., 1961: Atmospheric emission and opacity at millimeter wavelengths due to oxygen. J. Geophys. Res., 66, 3749-3757.
- Riogone, J. L. and A. P. Stogryn, 1977: Data processing for the DMSP Microwave Radiometer System. Eleventh International Symposium on Remote Sensing of the Environment, University of Michigan Press, 1-9.

- Rodgers, C. D., 1970: Remote sounding of the atmospheric temperature profile in the presence of cloud. Quart. J. Roy. Meteor. Soc., 96, 654-666.
- Savage, R. C., 1976: The Transfer of Thermal Microwaves Through Hydrometers. Doctor of Philosophy (Meteorology) Dissertation, University of Wisconsin-Madison, 10-15.
- Saxton, J. A. and J. A. Lane, 1952: Electrical properties of sea water: reflection and attenuation characteristics at v.h.f. Wireless Engineer, 29, 269-275.
- Sekhon, R. S. and R. C. Srivastava, 1970: Snow size spectra and radar reflectivity. J. Atmos. Sci., 27, 299-307.
- Smith, W. L. et al., 1970: A regression method for obtaining real-time temperature and geopotential height profiles from satellite spectrometer measurements and its application to Nimbus 3 SIRS observations. Mon. Wea. Rev., 98, 582-603.
- Staelin, D. H., et al., 1975: Microwave atmospheric temperature sounding: effects of clouds on the Nimbus 5 satellite data. J. Atmos. Sci., 32, 1970-1976.
- Waters, J. W., et al., 1975: Remote sensing of atmospheric temperature profiles with the Nimbus 5 microwave spectrometer. J. Atmos. Sci., 32, 1953-1969.

VITA

Name	Paul Thomas Nipko
Birthdate	March 14, 1948
Birthplace	Berlin, Wisconsin
High School	Berlin High School Berlin, Wisconsin
Universities	Wisconsin State University-Oshkosh Oshkosh, Wisconsin 1966-1967 United States Air Force Academy Colorado Springs, Colorado 1967-1971 Saint Louis University Saint Louis, Missouri 1971-1972 University of Utah Salt Lake City, Utah 1977-1979
Degree	B.S., 1971 United States Air Force Academy Colorado Springs, Colorado
Honorary Societies	Chi Epsilon Pi
Professional Position	Meteorologist, Officer United States Air Force

FILMED
8